



Article

Optimum Fractional Tilt Based Cascaded Frequency Stabilization with MLC Algorithm for Multi-Microgrid Assimilating Electric Vehicles

Abdullah M. Noman ¹, Mokhtar Aly ², Mohammed H. Alqahtani ^{1,*}, Sulaiman Z. Almutairi ¹, Ali S. Aljumah ¹, Mohamed Ebeed ³ and Emad A. Mohamed ^{1,4}

- ¹ Department of Electrical Engineering, College of Engineering, Prince Sattam bin Abdulaziz University, Al Kharj 16278, Saudi Arabia; a.noman@psau.edu.sa (A.M.N.); s.almutairi@psau.edu.sa (S.Z.A.); as.aljumah@psau.edu.sa (A.S.A.); e.younis@psau.edu.sa (E.A.M.)
- ² Facultad de Ingeniería, Arquitectura y Diseño, Universidad San Sebastián, Bellavista 7, Santiago 8420524, Chile; mokhtar.aly@uss.cl
- ³ Department of Electrical Engineering, Faculty of Engineering, Sohag University, Sohag 82524, Egypt; mebeed@eng.sohag.edu.eg
- ⁴ Department of Electrical Engineering, Faculty of Engineering, Aswan University, Aswan 81542, Egypt
- * Correspondence: mh.alqahtani@psau.edu.sa

Abstract: An important issue in interconnected microgrids (MGs) is the realization of balance between the generation side and the demand side. Imbalanced generation and load demands lead to security, power quality, and reliability issues. The load frequency control (LFC) is accountable for regulating MG frequency against generation/load disturbances. This paper proposed an optimized fractional order (FO) LFC scheme with cascaded outer and inner control loops. The proposed controller is based on a cascaded one plus tilt derivative (1+TD) in the outer loop and an FO tilt integrator-derivative with a filter (FOTIDF) in the inner loop, forming the cascaded (1+TD/FOTIDF) controller. The proposed 1+TD/FOTIDF achieves better disturbance rejection compared with traditional LFC methods. The proposed 1+TD/FOTIDF scheme is optimally designed using a modified version of the liver cancer optimization algorithm (MLCA). In this paper, a new modified liver cancer optimization algorithm (MLCA) is proposed to overcome the shortcomings of the standard Liver cancer optimization algorithm (LCA), which contains the early convergence to local optima and the debility of its exploration process. The proposed MLCA is based on three improvement mechanisms, including chaotic mutation (CM), quasi-oppositional based learning (QOBL), and the fitness distance balance (FDB). The proposed MLCA method simultaneously adjusts and selects the best 1+TD/FOTIDF parameters to achieve the best control performance of MGs. Obtained results are compared to other designed FOTID, TI/FOTID, and TD/FOTID controllers. Moreover, the contribution of electric vehicles and the high penetration of renewables are considered with power system parameter uncertainty to test the stability of the proposed 1+TD/FOTIDF LFC technique. The obtained results under different possible load/generation disturbance scenarios confirm a superior response and improved performance of the proposed 1+TD/FOTIDF and the proposed MLCA-based optimized LFC controller.

Keywords: electric vehicles (EVs); fractional order control; load frequency control; liver cancer algorithm; microgrids; optimum control design



Citation: Noman, A.M.; Aly, M.; Alqahtani, M.H.; Almutairi, S.Z.; Aljumah, A.S.; Ebeed, M.; Mohamed, E.A. Optimum Fractional Tilt Based Cascaded Frequency Stabilization with MLC Algorithm for Multi-Microgrid Assimilating Electric Vehicles. *Fractal Fract.* **2024**, *8*, 132. <https://doi.org/10.3390/fractalfract8030132>

Academic Editors: David Kubanek, Jie Wang, Bin Wang, Xin Li, Yang Zhou and Sunhua Huang

Received: 16 January 2024
Revised: 12 February 2024
Accepted: 19 February 2024
Published: 23 February 2024



Copyright: © 2024 by the authors. Licensee MDPI, Basel, Switzerland. This article is an open access article distributed under the terms and conditions of the Creative Commons Attribution (CC BY) license (<https://creativecommons.org/licenses/by/4.0/>).

1. Introduction

The stability of the power system has been a major issue for decades in interconnected power networks. It is defined as a power system's ability to stabilize itself following the elimination of disruptions. The smooth operation of the power system may be severely harmed if the synchronism is lost. The term stability is a measure of the reliability of the power system. That means the different parts of the power system should be kept synchronized to achieve high system reliability [1]. In some cases, different external conditions

may deviate the system from its stability region. Therefore, the control must maintain the power system frequency at a specific value in order to maintain the synchronism and hence keep the system stable [2]. Numerous frequency control systems have been proposed in the literature. This control is called load frequency control (LFC), in which the control regulates the system frequency at a stable level. Controlling the load/generation frequency is a challenging task in the interconnected power system since manual control is not possible [3]. The LFC study divides the interconnected power system into different control areas [4–6]. The condition is to maintain the same frequency of all generators in each area. Consequently, to ensure regular steady-state operation, the control area must maintain the power consumption of each region as well as the overall frequency of the system [7–9].

The large interconnected power system is characterized by large load centers and intricate dynamic structures, and hence the control system becomes more sophisticated [10,11]. These systems can be classified as conventional systems, in which the conventional energy sources are used such as thermal, hydro, gas, and nuclear [12,13]. The research on the use of LFC to enhance the performance of these large interconnected power systems started with single-area power systems with thermal units [14–16]. Afterward, the research was carried out with other sources, such as hydro, diesel generators, nuclear, etc., [17–19]. Then, the electric vehicle was included in the interconnected power system, and research was carried out on the effect of the electric vehicle on the frequency variations, and many controllers were proposed to solve these effects [20,21]. Furthermore, the research was extended to two-area with single, two, three, and multi-sources [22–24]. Moreover, the research was extended to three-area, four-area, and multi-area with two sources, three sources, and multisource as studied in [25–27].

From another point of view, the deployment of diverse renewable energy sources (RES) into power systems introduced new systems like microgrids (MGs) and smart grid technologies [28]. The interconnection of the power grid with the RESs makes the active power unpredictable and finally leads to frequency deviations. The variation in the frequency may lead to an unstable power system performance. In the literature, many studies have been conducted to create and enhance the design of LFCs [29–31].

LFC was previously obtained with traditional controllers in which Proportional-Integral-Derivative (PID) controllers represented the main control method. Different controllers have been proposed in the literature to improve the disadvantages of conventional controllers, such as high settling time, low rise time, and low accuracy [32]. The authors in [33] proposed a symbiotic organism search optimization technique to optimize the gains of the PID controller for a dual-area interconnected power grid. The authors in [34] proposed a backtracking search algorithm optimization technique to optimize the PI and PID controllers and enhance the LFC for the dual-area power system. The performance of the presented optimization technique is compared with the practical swarm optimization technique. The comparison results showed that the presented technique gives better results. The authors in [35] proposed a gravitational search algorithm for selecting for tuning the PID plus Filter (PIDF) for LFC of the dual-area power system. The presented algorithm improves the grid stability and reduces the oscillations. In [36], the binary moth flame optimization technique (MFO) with classical PI control was proposed to mitigate the system's frequency constraint issues. However, the effects and mitigation of RESs' effects have not been studied in this work.

The authors in [37] suggested quasi-oppositional Harris Hawks optimization for optimizing the constant of a suggested cascaded two-degree-of-freedom fractional order [FO(TDOF)] controller for the LFC of two areas, including PV, wind turbines, a biogas unit, and thermal unit power system. In the literature, fractional order controllers have improved system performance compared with traditional integer controllers [38–40]. The authors in [41] proposed a modified technique of chaotic-based atom search optimization for tuning the parameters of the fractional-order proportional integral derivative controller for the LFC of a multi-source hybrid power system including renewable energy sources. The writers in [42] proposed the offspring grey wolf optimization technique to tune the PID

controller gains and enhance its ability to pursue the random disturbance caused by the wind generator in the hydro-thermal-wind power network. The authors in [43] proposed a Modified Grey Wolf optimization algorithm hybrid with the Cuckoo search algorithm for optimal tuning the tilt integral derivative (TID) controller for a PV-thermal hybrid power generation.

Modern controllers, such as fuzzy logic controllers, neural network controllers, ANFIS controllers, sliding mode controllers, cascaded controllers, etc., were recently developed and used to control the load frequency [44–50]. The authors in [51] proposed a new cascaded proportional derivative plus proportional integral (PD-PI) technique. The presented controller is optimized using the gorilla troop optimization (GTO) technique for the LFC of a micro-grid that includes a diesel generator, wind turbines, PV, fuel cell, and electric vehicle. The authors in [50] proposed a new three-stage controller (PD-P-PID) for the FLC of single-area multisource and two-area multisource systems. The presented cascaded controller is optimized using the Marine Predators algorithm (MPA). The authors in [52] proposed a combination of the fractional model predictive controller (CFMPC) cascaded with the fractional-order PID controller (FOPID) for the LFC of dual-area power networks including PV and wind energy sources. In [53], a combination of PID and Fractional Order Proportional Integral Derivative (FOPID) control schemes with fractional derivative filters construct the proposed (PID/FOPIDFF). The presented controller is optimized based on a Slime Mold Algorithm (SMA), Gradient-based optimizer (GBO), and Hunger Games search optimizer (HGS).

In summary, the performance of LFC and the response of MG systems are highly determined by the type of LFC scheme, and the design methodology of the control system. Although research was developed in the area, the study and improvement of the MG response against renewable energy fluctuations, benefiting batteries of EV systems, and managing the response of different areas need more research development. Recently, the liver cancer optimization algorithm has been presented. Although it has proven superior performance in standard test functions, it did not give the expected performance with the LFC design. A modified version is proposed in this paper to enhance the LFC response. The main contribution of this work is summed up as follows:

- A new improved fractional order methodology is proposed in the paper for controlling frequency in multi-area RES-EV-based microgrid systems. The modified controller presents two cascaded inner and outer control loops based on 1+TD and FOTIDF, respectively, forming the proposed 1+TD/FOTIDF controller. Also, the proposed 1+TD/FOTIDF coordinates and controls EV batteries' participation in the frequency regulation process.
- A new modified liver cancer optimization algorithm (MLCA) is proposed to overcome the limitations of the conventional strategy of Liver cancer optimization algorithm (LCA). The proposed MLCA can avoid the early concourse to local optima and the debility of its exploration process. The proposed MLCA is based on three improvement mechanisms, including chaotic mutation (CM), quasi-oppositional based learning (QOBL), and the fitness distance balance (FDB).
- The proposed MLCA is applied to optimally determine the parameters of the proposed 1+TD/FOTIDF controller. The obtained results show a better response and mitigation of different step generation/loading changes compared to other optimization methods and/or conventional controllers.

The paper then is organized as follows: Section 2 presents MG description and components modeling with RES models and a complete systems state space model. The proposed 1+TD/FOTIDF LFC method and optimizing parameters with an overview of the existing literature on the LFCs and FO models are provided in Section 3. Section 4 details the proposed modified liver cancer optimization algorithm and its performance verification with its application in optimizing the proposed 1+TD/FOTIDF LFC. The obtained results of the LFC using the selected MGs system enhanced with performance comparison

and discussions are detailed in Section 5. Finally, the paper and results are concluded in Section 6.

2. MG Model and Description

2.1. MGs' Construction

Figure 1 shows the basic MG structure with the interconnection lines. The proposed 1+TD/FOTIDF control scheme is used in each area for controlling both existing generations and EV battery systems. It compensates for the power imbalance, which is reflected as deviations in system frequency and inter-areas tie-line power. In the studied MGs, RESs are distributed among interconnected areas considering wind generation in the first area (area *a*) and PV generation in the other area (Area *b*). The EVs are actively used through their inherent BESSs to participate during the frequency regulation process. The EVs are assumed to be equally divided between areas *a* and *b*. Additionally, conventional generation units are used in studied MGs by considering thermal plant units in area *a* and hydraulic plant units in area *b*. A MATLAB/SIMULINK jointed with an m-file is used for simulating the MGs with the proposed LFC. Complete MG element models are included in a single diagram as shown in Figure 2. Descriptions of various models are detailed in the following sub-sections.

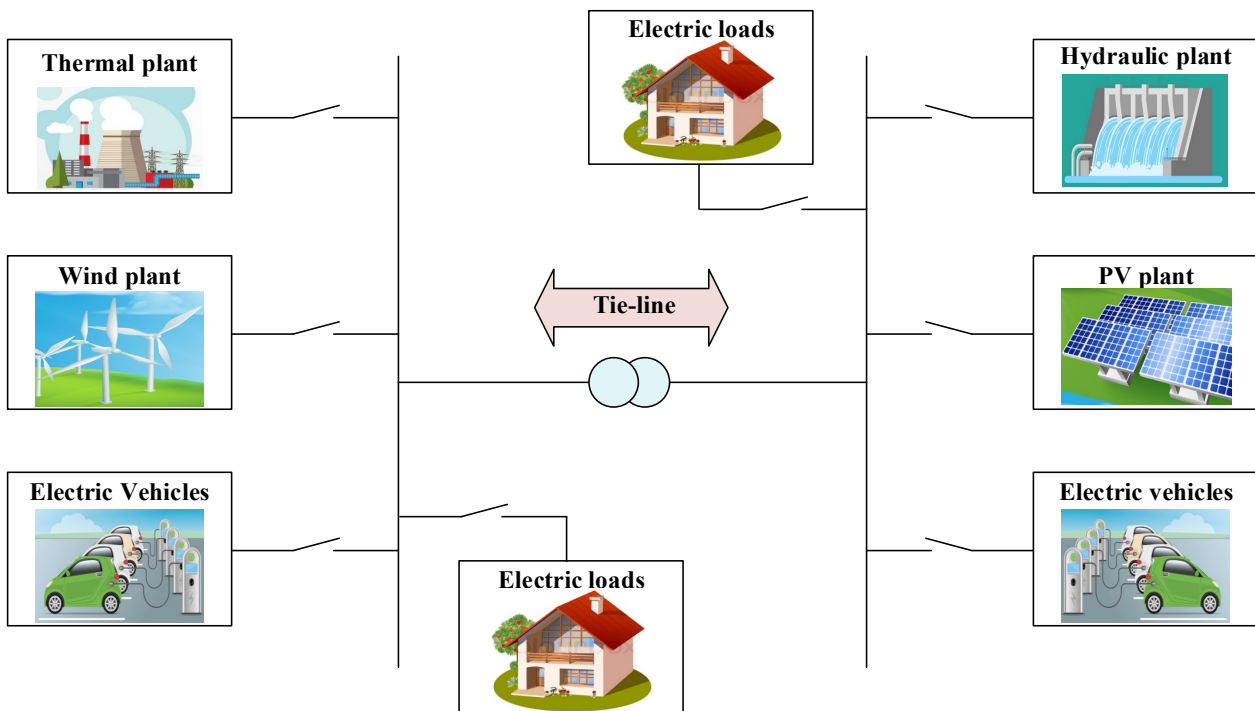


Figure 1. Main elements of the studied MG interconnected with RESs and EVs.

2.2. Modeling of Thermal and Hydraulic Generators

The model transfer function (TF) for thermal plant units is usually represented by the governor stage $G_g(s)$, and turbine stage $G_t(s)$ considering the nonlinearity of generation rate constraints (GRC) which is given as 0.3 pu MW/min for thermal and hydraulic power plants. The implemented TFs for $G_t(s)$, and $G_g(s)$ are represented as [54]:

$$G_g(s) = \frac{1}{T_g s + 1} \quad (1)$$

$$G_t(s) = \frac{1}{T_t s + 1} \quad (2)$$

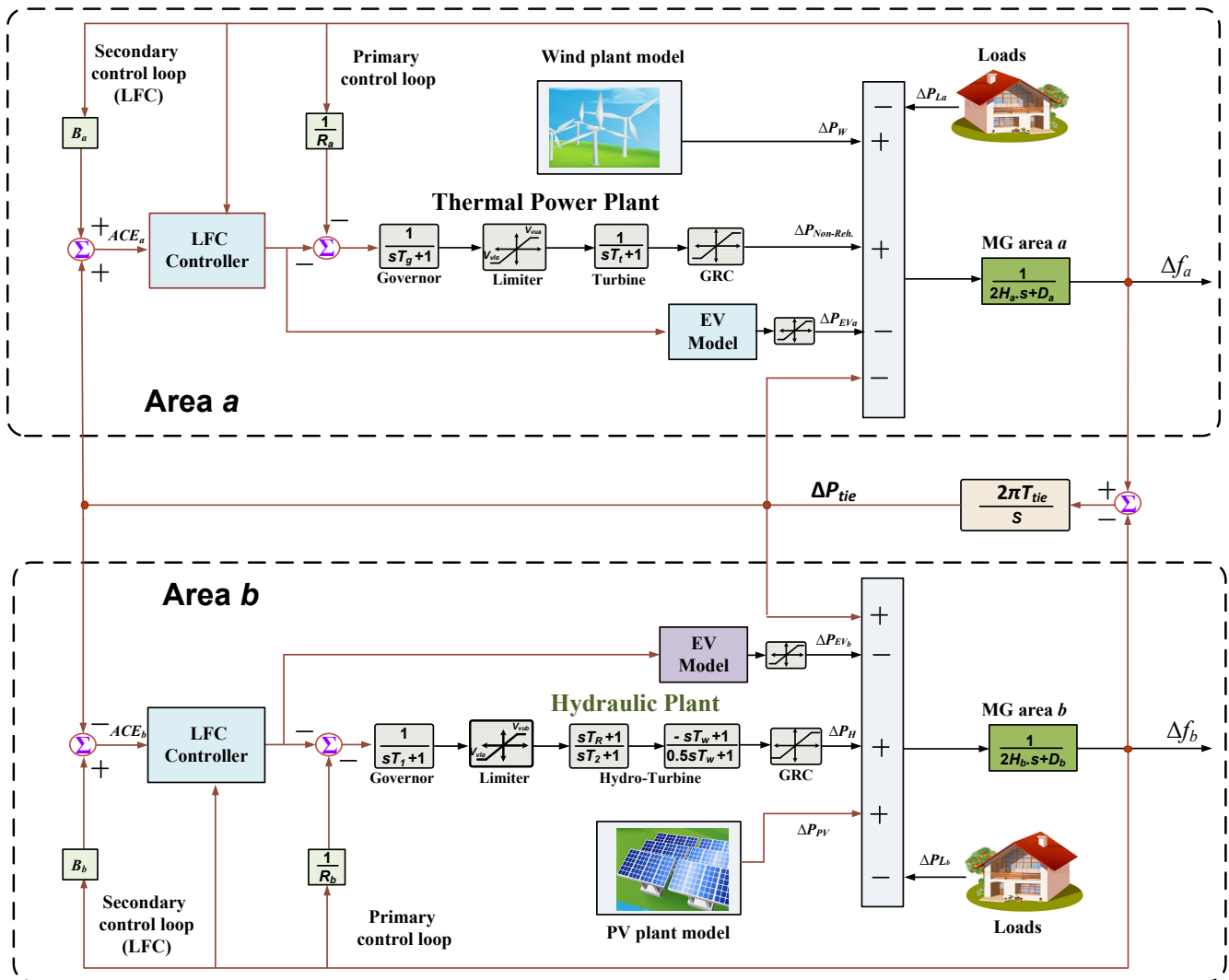


Figure 2. Modelling and representation of various components of interconnected MGs with RESs and EVs.

This leads to having the complete thermal plants model TF $G_T(s)$ as follows [55]:

$$G_T(s) = \frac{1}{T_g s + 1} \cdot \frac{1}{T_t s + 1} \quad (3)$$

The performance of the hydraulic turbines relies on the value of inertia, water's compressibility, and the pipes' wall elasticity. By 1977, the IEEE committee had recommended hydraulic turbines' mathematical modeling by assuming that the water flowing through penstock pipes is a non-compressible fluid and the water's velocity is proportionally dependent on the gate valve. The water's velocity in penstock pipes is represented as follows:

$$U = K_u \cdot G \cdot \sqrt{H_g} \frac{1}{T_t s + 1} \quad (4)$$

where U , H_g , and G are the proportionality constant, the hydraulic head, and the gate valve's position, respectively. The mechanical power from turbine P_m is represented as:

$$P_m = K_p \cdot H_g \cdot U \quad (5)$$

The required time for water to travel over L length of conduit with velocity U_0 and gravity acceleration a_g is expressed as;

$$T_w = \frac{LU_0}{a_g H_0} \quad (6)$$

Normally, hydraulic plants' TFs are modeled using the governor TF $G_{gh}(s)$, droop compensation TF $G_{gh}(s)$, and penstock turbines TF $G_{th}(s)$. The complete hydraulic TF $G_h(s)$ is represented as [56]:

$$G_h(s) = \frac{1}{T_1 s + 1} \cdot \frac{T_{RS} + 1}{T_2 s + 1} \cdot \frac{-T_w s + 1}{0.5 T_w s + 1} \quad (7)$$

The MGs' power system is usually modeled using first-order TF $G_{px}(s)$ as [56]:

$$G_{px}(s) = \frac{1}{2H_x s + D_x} \quad (8)$$

where H_x stands for areas inertia constants and D_x stands for areas damping constants.

2.3. Modeling EVs' BESSs

Figure 3 presents the implemented EV BESSs model. The proposed 1+TD/FOTIDF controller is employed in a centralized way in each area to control the existing generation units and the EV BESSs. The model contains a parallel RC branch using (R_t and C_t). The RC branch describes the various transient overvoltages of the EVs BESS. The resistance R_s is referred to as BESS thermal resistance. The regulation signal output from the regulation controller is transferred to the current to charge/discharge BESS using the P/V_{nom} term while considering the initial state of charge (SOC) in the model. With the recent concerns of replacing traditional transportation systems with EVs in various applications, the use of their BESSs can be used for the charge/discharge process based on grid conditions. Their participation can be leveraged to reduce the necessity for additional ESSs in MGs. The outputted V_{oc} of the EV model is related to the SOC of batteries (referred to $V_{oc}(SOC)$) based on the Nernst equation as follows [56]:

$$V_{oc}(SOC) = V_{nom} + S \frac{RT}{F} \ln \left(\frac{SOC}{C_{nom} - SOC} \right) \quad (9)$$

where V_{nom} is BESS's nominal voltage, C_{nom} is BESS's nominal capacity (Ah). The sensitivity parameter S between V_{oc} and BESS's SOC. The gas constant is denoted by R , the Faraday constant is represented by F , and temperature is represented by T .

2.4. Wind Plant's Model

Outputted wind power possesses intermittency due to its dependency on environmental conditions, such as wind speed, ambient temperature conditions, etc. The continuous variation in wind speed during the day affects the power output from wind plants. The mechanical power taken from wind (P_{WT}) is represented by [57]:

$$P_{WT} = \frac{1}{2} \rho A_T V_W^3 C_p(\lambda, \beta) \quad (10)$$

where, A_T blades swept area (in m^2), ρ stands for air density (in kg/m^3), V_W is wind speed (in m/s), and $C_p(\lambda, \beta)$ refers to power coefficient in function of tip-speed ratio λ and pitch angle of blades β . It provides an indication of how much power is extracted from the wind by the turbine. The $C_p(\lambda, \beta)$ is expressed as [57]:

$$C_p(\lambda, \beta) = 0.5 \left(\lambda_i - 0.022\beta^2 - 5.6 \right) e^{-0.17\lambda_i} \quad (11)$$

whereas, λ_i and λ are expressed as [57]:

$$\lambda_i = \frac{3600 \times R}{1609 \times R} \tag{12}$$

$$\lambda = \frac{\omega_B \times R}{V_W} \tag{13}$$

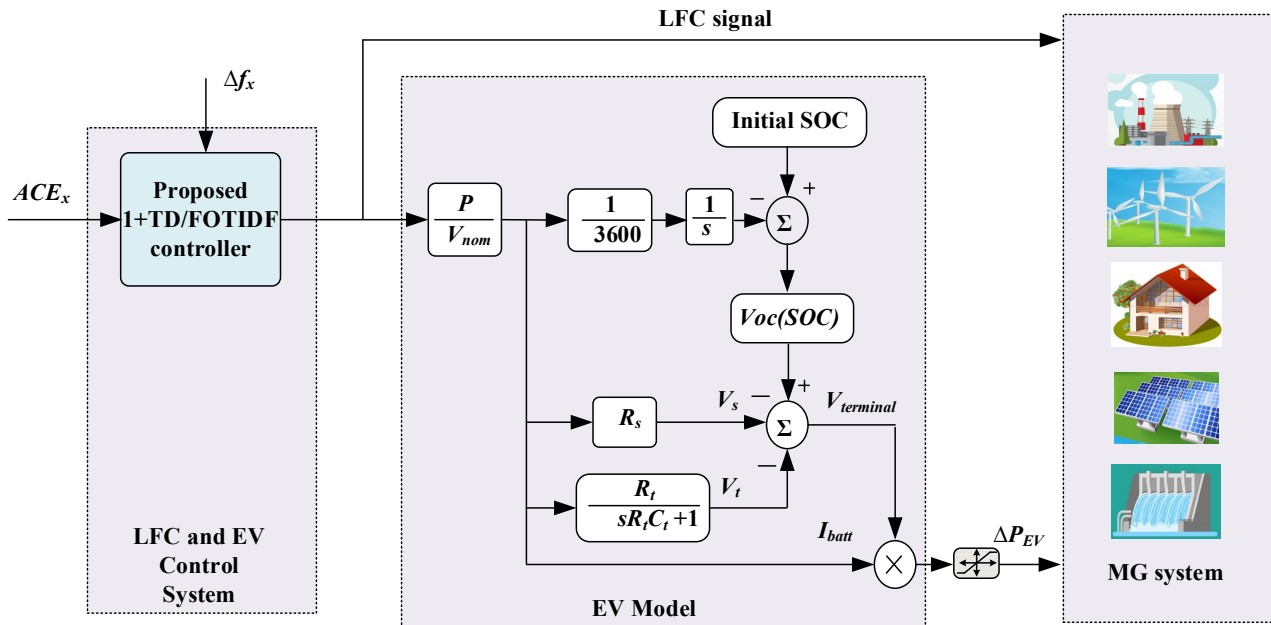


Figure 3. Modeling of EVs’ batteries participation in LFC function.

The continuously varying wind power is represented in this paper to count for wind power uncertainty. The outputted power from the model is then passed by the model of the inverter system as a first-order TF. The implemented TF of the wind plant $G_{WT}(s)$ is represented by [54]:

$$G_{WT}(s) = \frac{K_{WT}}{T_{WT}s + 1} \tag{14}$$

where K_{WT} is the gain symbol of the wind plant and T_{WT} is its associated time constant.

2.5. Modeling of PV Power Plants

A type of solar energy, known as solar PV, is one that uses the photo-electric effect to convert solar radiation into electrical power. Solar energy is coming from the sun and spread out into the space in the form of photons. When the photons strike the solar cells that connect the PV module, they transfer energy to the module, allowing negatively charged electrons to break free from their atoms. After absorbing photon energy, these electrons have enough energy to travel and head toward the opposite (negative) side of the panel, which is how the potential difference and electrical energy are produced.

The PV cell model seen in Figure 4 is employed to simulate the PV module. The open-circuit voltage (V_{oc}) and short-circuit current (I_{sc}) are determined under various weather conditions. The I_{sc} and the V_{oc} at standard weather conditions ($G_{st} = 1000 \text{ W/m}^2$ and $T_{st} = 25 \text{ }^\circ\text{C}$) can be obtained from the PV module’s nameplate. The generated current by the incident light (I_{PV}), which is called short-circuit current (I_{sc}), is determined at a given cell temperature (T_a) as follows [58,59]:

$$I_{PV} = I_{scn}(1 + a(T_a - T_n)) \frac{G}{G_n} \tag{15}$$

where I_{scn} represents Short circuit current at normal circumstances (25 °C, 1000 W/m²). T_a is the given cell temperature (K). a is the temperature coefficient of I_{sc} in percent change per degree temperature. G_n is the nominal value of irradiance, which is normally 1000 W/m². As seen from Figure 4, the output current delivered to the load can be expressed as [58,59]:

$$I = I_{PV} - I_0 \left(e^{\frac{q(V+IR_s)}{nKT_a}} - 1 \right) - \frac{V_D}{R_p} \quad (16)$$

where V_D is the diode voltage. The reverse saturation current of diode (I_{on}) at the reference temperature (T_n) is given as [58,59]:

$$I_{on} = \frac{I_{scn}}{e^{\frac{qV_{ocn}}{nKT_n}} - 1} \quad (17)$$

where V_{ocn} is the open circuit voltage at normal conditions. The reverse saturation current (I_o) at T_a is given as [58]:

$$I_o = I_{on} \left(\frac{T_a}{T_n} \right)^{\frac{3}{n}} e^{-\frac{qE_g}{nK} \left(\frac{1}{T_a} - \frac{1}{T_n} \right)} \quad (18)$$

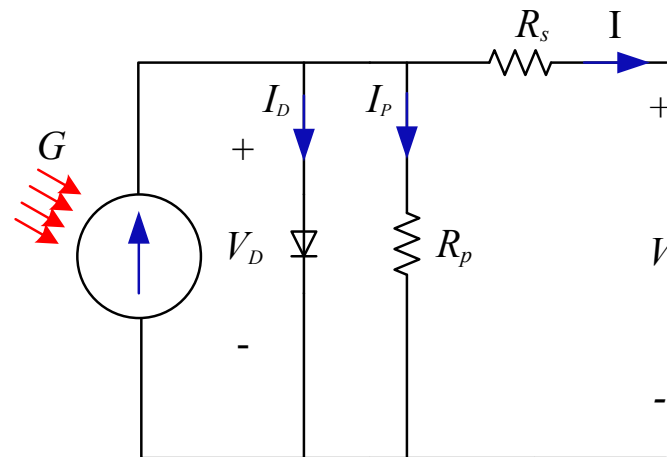


Figure 4. Equivalent single-diode model circuit of the PV cell.

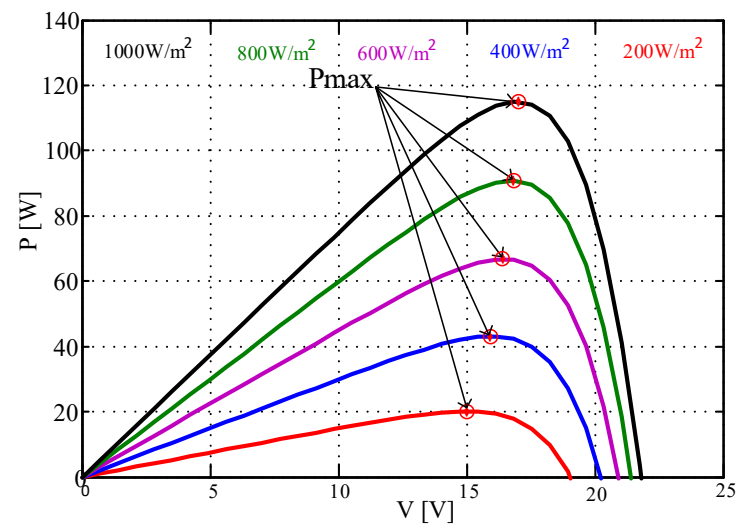
The series resistance (R_s) of the PV module has a large impact on the slope of the I-V curve near V_{oc} . The output voltage of the PV cell is given as:

$$V = V_D - IR_s \quad (19)$$

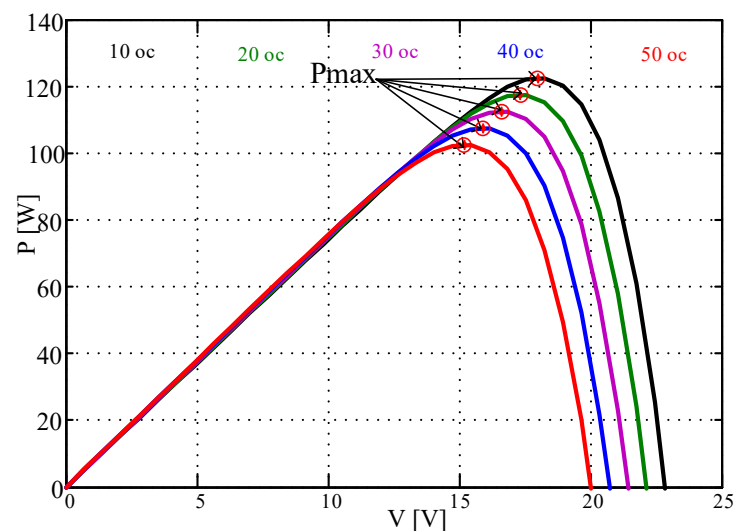
The PV module No. BP3115 is used in this paper. The PV module parameters at standard conditions (1000 W/m², 25 °C) are listed in Table 1. As seen in the previous equations, changing the ambient temperature and the irradiance level affects the performance of the PV module. To verify the output power ranges of the used PV module with changing weather conditions, the PV module model is simulated and tested under changes in solar radiation and changes in the PV cell temperature. The simulation results of the PV power versus PV voltage at different irradiance levels and cell temperatures are shown in Figure 5a,b, respectively. As can be noted in Figure 5a, when the solar radiation is increased from 200 W/m² to 1000 W/m² with 200 W/m² steps and at a constant cell temperature (25 °C), the maximum power point (MPP) is increased from approximately 20 W at 200 W/m² to 115 W at 1000 W/m², and the V_{oc} is slightly increased too. Moreover, the simulation results of the PV power versus PV voltage under different temperatures, 10 °C to 50 °C with 10 °C steps with constant solar radiation (1000 W/m²), are shown in Figure 5b. In these curves, the MPP is increased by reducing the cell temperature.

Table 1. The employed PV Module Parameters in the study.

Parameter	Value
Maximum Power value (P_{max})	115 W
Voltage at Maximum Power value (V_{mp})	17.1 V
Current at Maximum Power value (I_{mp})	6.7 A
Voltage value at Open-Circuit (V_{oc})	21.8 V
Current value at Short -Circuit (I_{sc})	7.5 A



(a)



(b)

Figure 5. P-V curves as a function of ambient conditions. (a) With irradiance level variations; (b) With temperature variations.

The inverter system of PV generation is also included in the model using the TF $G_{PV}(s)$ and it is modeled as [60]:

$$G_{PV}(s) = \frac{K_{PV}}{T_{PV}s + 1} \quad (20)$$

where, K_{PV} and T_{PV} refer to the gain, and the time constant of the PV power plant inverter system, respectively.

2.6. MG's Complete Model

The complete studied MG's system is shown in Figure 2. The system can be linearized and jointly represented in a single-state space model. The state space model is generally expressed as:

$$\dot{x} = Ax + B_1\omega + B_2u \tag{21}$$

$$y = Cx \tag{22}$$

where x is the vector of state variables, y is the vector of output states, ω includes the disturbances vector, and u includes control variables. A , B_1 , B_2 , and C are the obtained system parameters' matrices in the linear state-space representation of the two-area power system. The representations of x and ω are conducted as:

$$x = [\Delta f_a \ \Delta P_{ga} \ \Delta P_{ga1} \ \Delta P_{WT} \ \Delta f_b \ \Delta P_{gb} \ \Delta P_{gb1} \ \Delta P_{gb2} \ \Delta P_{PV} \ \Delta P_{tie,ab}]^T \tag{23}$$

$$\omega = [\Delta P_{la} \ P_{WT} \ \Delta P_{lb} \ P_{PV}]^T \tag{24}$$

Control variables u include output from each controller ($C_{out,a}$ and $C_{out,b}$) and EV side power demand/injection (ΔP_{EVa} and ΔP_{EVb}) based on charge/discharge commands. The control variables u are expressed as:

$$u = [C_{out,a} \ \Delta P_{EVa} \ C_{out,b} \ \Delta P_{EVb}]^T \tag{25}$$

System component representations are included in the state-space model using the matrices (A , B_1 , B_2 , and C). Their representation of studied MG systems is as follows:

$$A = \begin{bmatrix} -\frac{D_a}{2H_a} & \frac{1}{2H_a} & 0 & \frac{1}{2H_a} & 0 & 0 & 0 & 0 & 0 & -\frac{1}{2H_a} \\ 0 & -\frac{1}{T_i} & \frac{1}{T_i} & 0 & 0 & 0 & 0 & 0 & 0 & 0 \\ -\frac{1}{R_a T_g} & 0 & -\frac{1}{T_g} & 0 & 0 & 0 & 0 & 0 & 0 & 0 \\ 0 & 0 & 0 & -\frac{1}{T_{WT}} & 0 & 0 & 0 & 0 & 0 & 0 \\ 0 & 0 & 0 & 0 & -\frac{D_b}{2H_b} & \frac{1}{2H_b} & 0 & 0 & \frac{1}{2H_b} & \frac{1}{2H_b} \\ 0 & 0 & 0 & 0 & \frac{2T_R}{R_b T_1 T_2} & -\frac{2}{T_w} & \frac{2T_2 + 2T_w}{T_2 T_w} & \frac{2T_R - 2T_1}{T_1 T_2} & 0 & 0 \\ 0 & 0 & 0 & 0 & -\frac{T_R}{R_b T_1 T_2} & 0 & -\frac{1}{T_2} & \frac{T_1 - T_R}{T_1 T_2} & 0 & 0 \\ 0 & 0 & 0 & 0 & -\frac{1}{R_b T_1} & 0 & 0 & -\frac{1}{T_1} & 0 & 0 \\ 0 & 0 & 0 & 0 & 0 & 0 & 0 & 0 & -\frac{1}{T_{PV}} & 0 \\ 2\pi T_{tie,eq} & 0 & 0 & 0 & -2\pi T_{tie,eq} & 0 & 0 & 0 & 0 & 0 \end{bmatrix} \tag{26}$$

$$B_1 = \begin{bmatrix} -\frac{1}{2H_a} & 0 & 0 & 0 \\ 0 & 0 & 0 & 0 \\ 0 & 0 & 0 & 0 \\ 0 & \frac{K_{WT}}{T_{WT}} & 0 & 0 \\ 0 & 0 & -\frac{1}{2H_b} & 0 \\ 0 & 0 & 0 & 0 \\ 0 & 0 & 0 & 0 \\ 0 & 0 & 0 & 0 \\ 0 & 0 & 0 & \frac{K_{PV}}{T_{PV}} \\ 0 & 0 & 0 & 0 \end{bmatrix}, \quad \text{and} \quad B_2 = \begin{bmatrix} 0 & -\frac{1}{2H_a} & 0 & 0 \\ 0 & 0 & 0 & 0 \\ -\frac{1}{T_g} & 0 & 0 & 0 \\ 0 & 0 & 0 & 0 \\ 0 & 0 & 0 & -\frac{1}{2H_b} \\ 0 & 0 & \frac{2T_R}{T_1 T_2} & 0 \\ 0 & 0 & -\frac{T_R}{T_1 T_2} & 0 \\ 0 & 0 & -\frac{1}{T_1} & 0 \\ 0 & 0 & 0 & 0 \\ 0 & 0 & 0 & 0 \end{bmatrix} \tag{27}$$

$$C = \begin{bmatrix} 1 & 0 & 0 & 0 & 0 & 0 & 0 & 0 & 0 & 0 \\ B_a & 0 & 0 & 0 & 0 & 0 & 0 & 0 & 0 & 1 \\ 0 & 0 & 0 & 0 & 1 & 0 & 0 & 0 & 0 & 0 \\ 0 & 0 & 0 & 0 & B_b & 0 & 0 & 0 & 0 & -1 \end{bmatrix} \tag{28}$$

The implemented models use the parameters presented in [54]. Table 2 summarizes the employed parameters for the developed modeling of interconnected MG components.

Table 2. Used Parameters for representing MGs system (with $x \in \{a, b\}$), [54].

Parameters	Symbols	Value	
		Area <i>a</i>	Area <i>b</i>
Rated MGs' capacity	P_{rx} (MW)	1200	1200
Droops constant	R_x (Hz/MW)	2.4	2.4
Frequency bias values	B_x (MW/Hz)	0.4249	0.4249
Valve gate limiting value (minimum)	V_{vlx} (p.u.MW)	−0.5	−0.5
Valve gate limiting value (maximum)	V_{vux} (p.u.MW)	0.5	0.5
Time constant for thermal governor	T_g (s)	0.08	-
Thermal turbines' (time constant)	T_t (s)	0.3	-
Governor of hydraulic generator (time constant)	T_1 (s)	-	41.6
Transient droops time constant for hydraulic governor	T_2 (s)	-	0.513
Governor of hydraulic generator resetting time	T_R (s)	-	5
Hydraulic turbines' water starting time	T_w (s)	-	1
Inertia's constants	H_x (p.u.s)	0.0833	0.0833
Damping coefficient	D_x (p.u./Hz)	0.00833	0.00833
PV generations time constant	T_{PV} (s)	-	1.3
PV generations' gains	K_{PV} (s)	-	1
Wind generations' time constants	T_{WT} (s)	1.5	-
Wind generations' gains	K_{WT} (s)	1	-
EV BESSs' models			
Penetration level	-	10%	10%
BESS voltages (nominal)	V_{nom} (V)	364.8	364.8
BESS capacity	C_{nom} (Ah)	66.2	66.2
Series resistances	R_s (ohms)	0.074	0.074
Transient resistance	R_t (ohms)	0.047	0.047
Transient capacitances	C_t (farad)	703.6	703.6
Constants value	RT/F	0.02612	0.02612
BESS's SOC (maximum)	%	95	95
BESS's energy capacity	C_{batt} (kWh)	24.15	24.15

3. Overview of LFC and FO Operators

3.1. LFC Schemes in Literature

As explained in the literature review, numerous integer order (IO), fractional order (FO), and hybrid IO-FO LFCs have been proposed in the literature. In general, IO-based control schemes have found wide employment in several frequency regulation controllers. The I, PI, ID, PID, PIDD, PID, and PIDF are examples of vastly applied IO LFC in literature. The TF representation $C(s)$ of these controllers are as follows [54–57]:

$$\begin{aligned}
 C_{PI}(s) &= \frac{Y(s)}{E(s)} = K_p + \frac{K_i}{s} \\
 C_{PIDD}(s) &= \frac{Y(s)}{E(s)} = K_p + \frac{K_i}{s} + K_{d1} s + K_{d2} s^2 \\
 C_{PID}(s) &= \frac{Y(s)}{E(s)} = K_p + \frac{K_i}{s} + K_d s \\
 C_{PIDF}(s) &= \frac{Y(s)}{E(s)} = K_p + \frac{K_i}{s} + K_d s \frac{N_f}{s+N_f}
 \end{aligned} \tag{29}$$

For instance, K_i , K_p , and K_d represent PID gains for integral, proportional, and derivative branches. They represent the flexibility of the PID LFC design process to optimize the MGs' frequency regulation functionality. The PIDF possesses the filter gain as an additional design flexibility parameter. Figure 6 shows the representation of the most common IO LFC in literature.

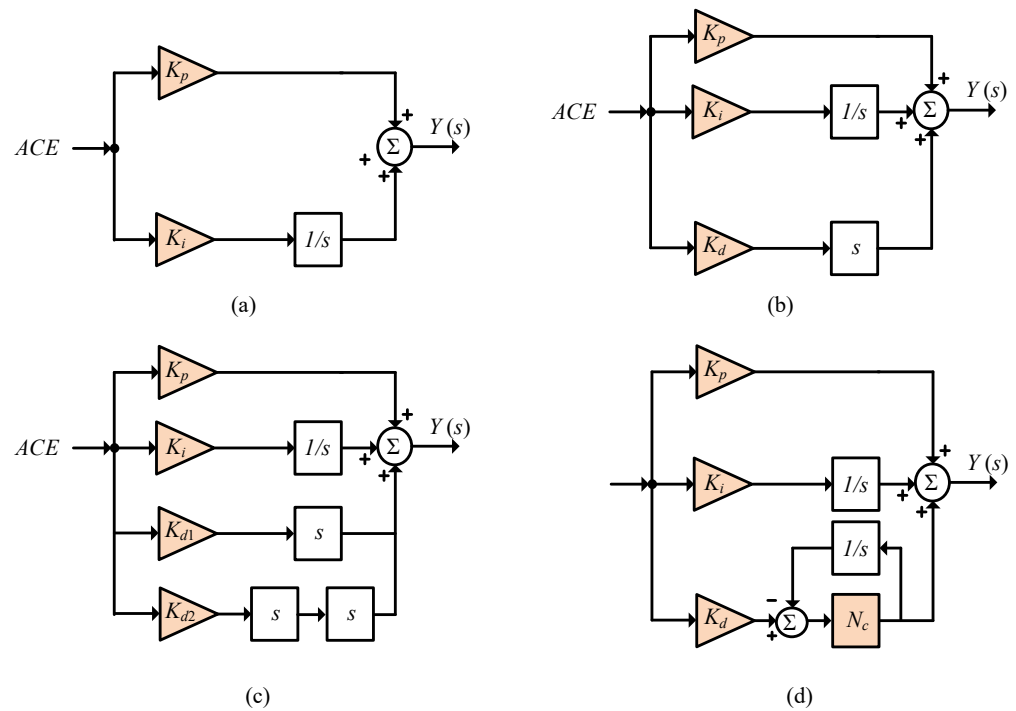


Figure 6. Literature examples of IO LFC (tunable LFC gains are colored): (a) PI; (b) PID; (c) PIDD; (d) PIDF.

On the other hand, FO-based LFC schemes have been presented to benefit from FO operators and their associated flexibility. The added FO integrator operator and FO derivative operator increase the DOF of LFC systems. Figure 7 shows some examples of existing FO LFC in literature. Some examples of existing FO LFC in literature are represented as [54–57]:

$$\begin{aligned}
 C_{FOPI}(s) &= \frac{Y(s)}{E(s)} = K_p + \frac{K_i}{s^\lambda} \\
 C_{TID}(s) &= \frac{Y(s)}{E(s)} = K_t s^{-(\frac{1}{n})} + \frac{K_i}{s} + K_d s \\
 C_{FOPID}(s) &= \frac{Y(s)}{E(s)} = K_p + \frac{K_i}{s^\lambda} + K_d s^\mu \\
 C_{TIDF}(s) &= \frac{Y(s)}{E(s)} = K_t s^{-(\frac{1}{n})} + \frac{K_i}{s} + K_d s \frac{N_f}{s+N_f}
 \end{aligned}
 \tag{30}$$

From Equation (30), the FO-based LFC includes the added FO operators (λ for integrator, and μ for derivative) to the gains (K_p , K_t , K_i , and K_d), which is reflected as more freedom in optimizing MG frequency regulation response. The FO operators in Equation (30) are usually tuned in the range of [0, 1].

3.2. FO Operators Representation

An important issue of FO control is the way to implement and represent FO operators using available digital control platforms. There are several definitions for FO calculus, such as the Caputo definition, the Grunwald–Letnikov definition, and the Riemann–Liouville definition [61]. In the definition of Grunwald–Letnikov, α_{th} is used as a fractional derivative to function f inside a to t limits. It is represented as [62]:

$$D^\alpha |^t_a = \lim_{h \rightarrow 0} \frac{1}{h^\alpha} \sum_{r=0}^{\frac{t-a}{h}} (-1)^r \binom{n}{r} f(t-rh)
 \tag{31}$$

In which, h is referred to as step time and $[\cdot]$ in integer terms' operator for the Grunwald–Letnikov definition. In (36), n lies in the range $(n - 1 < \alpha < n)$. Also, binomial coefficients can be expressed as [62]:

$$\binom{n}{r} = \frac{\Gamma(n + 1)}{\Gamma(r + 1)\Gamma(n - r + 1)} \tag{32}$$

where the function of gamma in (32) is normally defined as [61]:

$$\Gamma(n + 1) = \int_0^\infty t^{x-1} e^{-t} dt \tag{33}$$

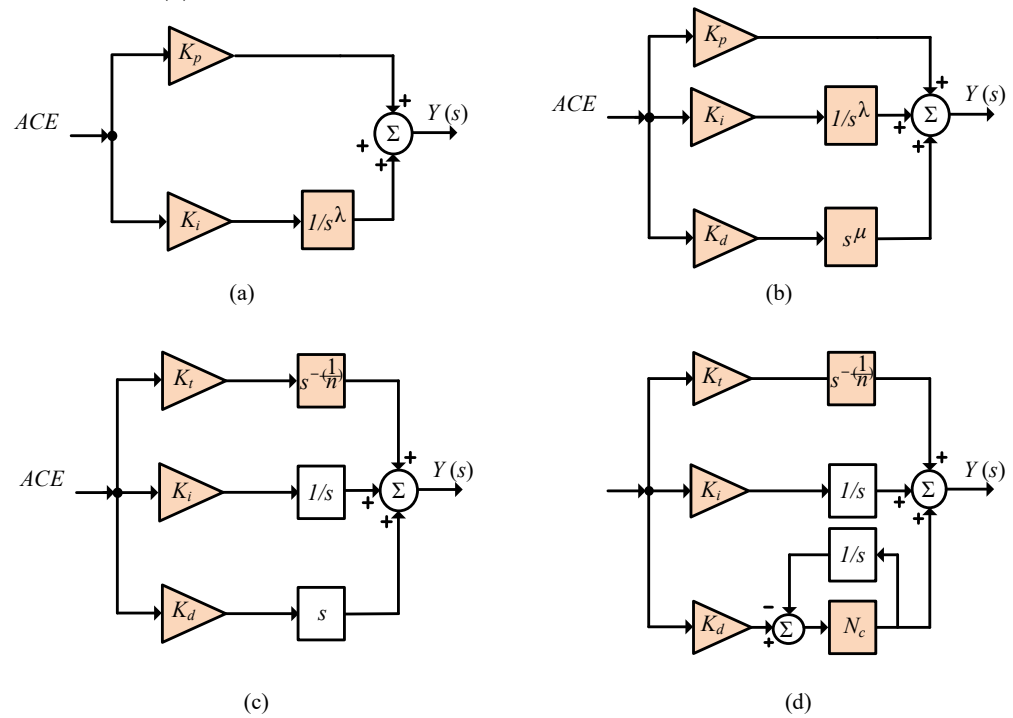


Figure 7. Literature examples of FO LFC (tunable LFC gains are colored): (a) FOPI; (b) FOPID; (c) TID; (d) FOTIDF.

The definition of Riemann–Liouville avoids the sum and limits. It employs the integer-based derivative and integral terms as [63]:

$$D^\alpha|_a^t = \frac{1}{\Gamma(n - \alpha)} \left(\frac{d}{dt} \right)^n \int_a^t \frac{f(\tau)}{(t - \tau)^{\alpha - n + 1}} d\tau \tag{34}$$

The definition of Caputo is represented as [62]:

$$D^\alpha|_a^t = \frac{1}{\Gamma(n - \alpha)} \int_a^t \frac{f^{(n)}(\tau)}{(t - \tau)^{\alpha - n + 1}} d\tau \tag{35}$$

Additionally, general FO operators are through employing $D^\alpha|_a^t$ as follows:

$$D^\alpha|_a^t = \begin{cases} \alpha > 0 \rightarrow \frac{d^\alpha}{dt^\alpha} & \text{FOderivative} \\ \alpha < 0 \rightarrow \int_{t_0}^t dt^\alpha & \text{FOintegral} \\ \alpha = 0 \rightarrow 1 \end{cases} \tag{36}$$

For the proper implementation using digital control processors, Oustaloup recursive approximation (ORA) has verified superior performance for implementing FO operators

using digital processors [61]. The ORA representation is employed in this work for implementing FO controllers. The α^{th} FO based derivative (s^α) is mathematically-approximated as [61]:

$$s^\alpha \approx \omega_h^\alpha \prod_{k=-N}^N \frac{s + \omega_k^z}{s + \omega_k^p} \quad (37)$$

where ω_k^p and ω_k^z refer to the locations of poles, and zeros, respectively, for the ω_h sequence. The calculations are performed as follows:

$$\omega_k^z = \omega_b \left(\frac{\omega_h}{\omega_b} \right)^{\frac{k+N+\frac{1-\alpha}{2}}{2N+1}} \quad (38)$$

$$\omega_k^p = \omega_b \left(\frac{\omega_h}{\omega_b} \right)^{\frac{k+N+\frac{1+\alpha}{2}}{2N+1}} \quad (39)$$

$$\omega_h^\alpha = \left(\frac{\omega_h}{\omega_b} \right)^{\frac{-\alpha}{2}} \prod_{k=-N}^N \frac{\omega_k^p}{\omega_k^z} \quad (40)$$

The existing poles/zeros number for the approximated FO ORA representation is $(2N + 1)$, and N defines the ORA order. The utilized ORA representation in this work is performed using ($M = 5$) within ($\omega \in [\omega_b, \omega_h]$) between $[10^{-3}, 10^3]$ rad/s frequency limits.

3.3. Proposed 1+TD/FOTIDF LFC

From the above-mentioned discussion about existing LFC in the literature, and the associated extra flexibility of using FO operators, this paper proposed a hybrid IO with the FO-based LFC method. The conventional IO and FO structures use the ACE feedback signal as an input for the controller. This leads to a slower response in these LFC schemes. Moreover, their ability to mitigate existing disturbances due to load and/or generation changes is poor. The proposed controller is based on the cascaded LFC methods. It uses two cascaded LFC loops in its structure. The 1+TD is used in implementing the outer controller loop by using the ACE signal as a feedback signal to this stage. The second loop uses the frequency deviation in each area as a feedback signal employing the FOTIDF in this loop. Therefore, the proposed LFC control is based on a 1+TD/FOTIDF controller with two feedback signals in each area (ACE and Δf_x). Figure 8 presents the proposed 1+TD/FOTIDF controller for interconnected MGs.

It can be seen that the proposed 1+TD/FOTIDF combines the benefits of IO with FO control systems. Adding 1 to the TD controller and cascading it with the FOTIDF controller leads to reducing the control complexity and facilitating the parameter determination compared with using the proportional term as proven in [64,65]. Additionally, it uses two different inner signals to the outer and inner control loops (ACE_a and Δf_a in area a) and (ACE_b and Δf_b in area b). The use of ACE_a and ACE_b in outer loops enables the proposed LFC method to mitigate the low-frequency disturbances in the systems. The use of Δf_a and Δf_b in inner loops enables the mitigation of existing high-frequency disturbances in MG systems. Therefore, improved disturbance rejection capability is obtained through proposed cascaded 1+TD/FOTIDF loops.

The input to the outer loop is ACE signals of each area ((ACE_a) , and (ACE_b)), which are expressed as error signals for the outer loop as $E_{a1}(s)$ and $E_{b1}(s)$, respectively, in this stage. These inputs are represented as:

$$\begin{aligned} E_{a1}(s) &= ACE_a = \Delta P_{tie} + B_a \Delta f_a \\ E_{b1}(s) &= ACE_b = A_{ab} \Delta P_{tie} + B_b \Delta f_b \end{aligned} \quad (41)$$

where (A_{ab}) refers to the capacity ratio among MGs areas a and b . The outputted control signals from this stage are $Y_{a1}(s)$ and $Y_{b1}(s)$. The representation of this outer loop is made as follows:

$$\begin{aligned} Y_{a1}(s) &= \left[1 + K_{t1} s^{-\left(\frac{1}{n_1}\right)} + K_{d1} s \right] \cdot E_{a1}(s) \\ Y_{b1}(s) &= \left[1 + K_{t3} s^{-\left(\frac{1}{n_3}\right)} + K_{d3} s \right] \cdot E_{b1}(s) \end{aligned} \tag{42}$$

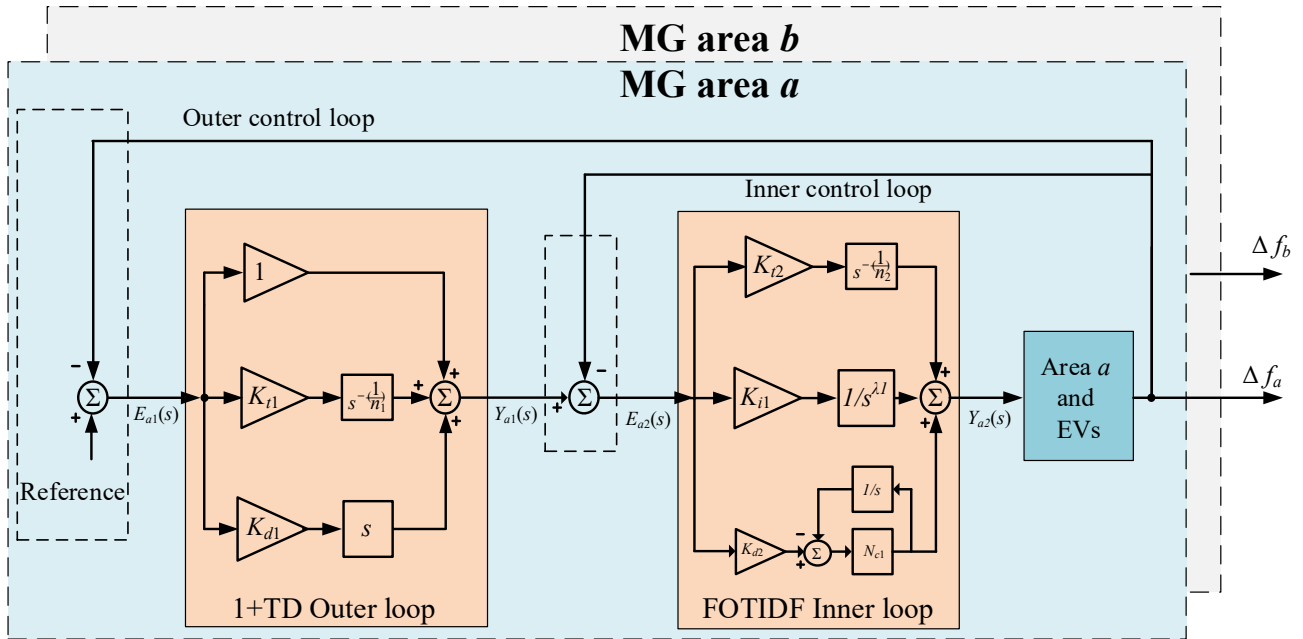


Figure 8. Structure of proposed 1+TD/FOTIDF LFC scheme.

From Equation (48), each MG outer loop has three tunable control parameters, which gives six total tunable parameters in the studied two areas. In MG area a , the three tunable control parameters are $(K_{t1}, K_{d1}$, and $n_1)$ inside the 1+TD controller loop. For MG area b , the tunable parameters are $(K_{t3}, K_{d3}$, and $n_3)$.

The output of the first outer loop is fed with frequency deviation signals $(\Delta f_a$, and $\Delta f_b)$ to the outer control stage. The error of the inputted signals $E_{a2}(s)$ and $E_{b2}(s)$ for second inner loop are represented as:

$$E_{a2}(s) = Y_{a1}(s) - \Delta f_a E_{b2}(s) = Y_{b1}(s) - \Delta f_b \tag{43}$$

In the inner loop, the FOTIDF is utilized in this stage. The control output $(Y_{a2}(s)$ and $Y_{b2}(s))$ is expressed as:

$$\begin{aligned} Y_{a2}(s) &= \left[1 + K_{t2} s^{-\left(\frac{1}{n_2}\right)} + \frac{K_{i1}}{s^{\lambda_1}} + K_{d2} \frac{N_{c1}}{s+N_{c1}} \right] \cdot E_{a2}(s) \\ Y_{b2}(s) &= \left[1 + K_{t4} s^{-\left(\frac{1}{n_4}\right)} + \frac{K_{i2}}{s^{\lambda_2}} + K_{d4} \frac{N_{c2}}{s+N_{c2}} \right] \cdot E_{b2}(s) \end{aligned} \tag{44}$$

From Equation (50), the MG area a has six tunable parameters $(K_{t2}, n_2, K_{i1}, \lambda_1, K_{d2}$, and $N_{c2})$ for designing its inner controller. MG area b has $(K_{t4}, n_4, K_{i2}, \lambda_2, K_{d4}$, and $N_{c2})$ tunable design parameters. There are a total of 12 tunable design parameters in the inner stage. Accordingly, the total representation of the proposed 1+TD/FOTIDF controller can be expressed as:

$$Y_{a2}(s) = \left[\left(1 + K_{t1} s^{-\left(\frac{1}{n_1}\right)} + K_{d1} s \right) A C E_a - \Delta f_a \right] \cdot \left[1 + K_{t2} s^{-\left(\frac{1}{n_2}\right)} + \frac{K_{i1}}{s^{\lambda_1}} + K_{d2} \frac{N_{c1}}{s+N_{c1}} \right] \tag{45}$$

$$Y_{b2}(s) = \left[\left(1 + K_{t3} s^{-\left(\frac{1}{n_3}\right)} + K_{d3} s \right) ACE_b - \Delta f_b \right] \cdot \left[1 + K_{t4} s^{-\left(\frac{1}{n_4}\right)} + \frac{K_{i2}}{s^{\lambda_2}} + K_{d4} \frac{N_{c2}}{s + N_{c2}} \right] \quad (46)$$

4. The Proposed Modified Liver Cancer Optimization Algorithm and Its Performance Verification

4.1. Liver Cancer Optimization Algorithm

The liver cancer optimization algorithm (LCA) is a developed optimizer that simulates liver tumor takeover and growth progression [66]. The LCA consists of several stages which are conceptualized from liver tumors and these stages can be defined as follows:

4.1.1. Tumor Size Estimation

It is important to calculate the size of the tumor for the following stages. For assigning the size of the tumor, it is assumed that the tumor has a hemi-ellipsoid shape, length, width and height. The initial tumor volume (location) can be calculated based on random opposition-based learning (ROBL) as follows:

$$X_i^{0j} = \frac{\pi}{6} (Le^j) \cdot (Wi^j) \cdot (Hi^j) - \left(Ib + (ub - Ib) - r_d \times X_i^j \right) \quad (47)$$

where X_i^{0j} is a vector that is opposite to X_i^j . Ib and ub represent the lower and the upper boundaries of variables. Le , Wi and Hi represent the length, the width and the height of the tumor, respectively. r_d represents a random value within $[0, 1]$. The height and width represent random factors in the range $[0-1]$. The increase in the tumor volume can be described as follows:

$$X = \frac{\pi}{6} \cdot f \cdot (Le \cdot Wi)^{3/2} \quad (48)$$

where f is the constant value that equals 1.

4.1.2. Tumor Replication

This stage is considered a dangerous stage of the tumor and is manipulated in many places in the liver where hepatocellular carcinoma increases exponentially. The volume or the location of the tumor in this stage can be assigned as follows:

$$p^i = \frac{dV}{dt} = r \times X \in [1...T] \text{ and } i \in [1...N] \quad (49)$$

where P refers to the tumor growth location. T denotes the maximum iteration number while N refers to the population numbers. The spread of the tumor in the liver can be found by the levy flight mechanism as follows:

$$v(D) = 0.01 \times \frac{\text{rand}(1, D) \times \sigma}{|\text{rand}(1, D)|^{\frac{1}{\beta}}} \quad (50)$$

$$= \left(\frac{\Gamma(1 + \beta) \times \sin\left(\frac{\pi\beta}{2}\right)}{\Gamma\left(\frac{1+\beta}{2}\right) \times \beta \times 2\left(\frac{\beta-1}{2}\right)} \right)^{\frac{1}{\beta}} \quad (51)$$

In this stage, LCA used the tumor-spreading mechanism and picked the best portion of the liver to assess its situation and determine the next procedure. This action can be mathematically represented as follows:

$$y = X + P \quad (52)$$

$$Z = Y + S \times LF(D) \quad (53)$$

$$X_{t+1}^i = \begin{cases} y & \text{if } fit(y) < fit(X_t^i) \\ z & \text{if } fit(z) < fit(X_t^i) \end{cases} \quad (54)$$

where D represents the dimensions of the problem. S is a random vector in $[0-1]$. fit refers to the fitness function.

4.1.3. Tumor Spreading

This stage is conceptualized by the spreading of the tumor to other body organs. Two operators are used to describe the spreading of the tumor including the mutation and the crossover. In the mutation operator, the populations will update their locations based on the mutation rate (ϵ), in which two vectors y and z were used to update the locations of the old vector if its random values are less than the mutation rate. The mutation process of the LCA can be described as follows:

$$y_{Mut} = \begin{cases} X & \text{if } r_1 \geq \epsilon \\ y & \text{else} \end{cases} \quad (55)$$

$$z_{Mut} = \begin{cases} X & \text{if } r_2 \geq \epsilon \\ z & \text{else} \end{cases} \quad (56)$$

In which,

$$\epsilon = \frac{t}{T}; \quad (57)$$

$$y = |X - X_t^j| \quad (58)$$

$$z = y - S \quad (59)$$

where, S has D elements captured from random values within $[0, 1]$. In the crossover, a new vector is generated by a combination of two individuals as described in the following equations:

$$X_{Cros} = \tau \times y_{Mut} + (1 - \tau') \times z_{Mut}, \tau \neq \tau' \quad (60)$$

where τ' and τ are random vectors. The locations of the newly updated tumors will be updated based on the fitness function values as follows:

$$X_{t+1}^i = \begin{cases} y_{Mut} & \text{if } fit(y_{Mut}) < fit(X^i) \\ z_{Mut} & \text{if } fit(z_{Mut}) < fit(X^i) \\ X_{Cros} & \text{if } fit(X_{Cros}) < fit(X^i) \end{cases} \quad (61)$$

4.2. The Proposed Modified Liver Cancer Algorithm

The proposed MLCA is based on enhancing the performance of the standard LCA using three modifications including the fitness distance balance (FDB), and the quasi-oppositional based learning (QOBL).

4.2.1. The FDB Method

The FDB is an efficient selection strategy that was applied to numerous optimization methods for performance improvement [67–72]. The FDB is based on updating the current populations based on the distance that was determined between the best solution and the current candidates as well as its fitness value. The corresponding distance of the FDB can be expressed as follows:

$$Dis_i = \sqrt{(X_i^1 - X_{best,1})^2 + (X_i^2 - X_{best,2})^2 + \dots + (X_i^d - X_{best,d})^2} \quad (62)$$

where X_{best1} is the best solution while X_i^j is the current solution. The distance and the fitness function values are represented as vectors as follows:

$$Obj = [Obj_1, Obj_2, \dots, Obj_n] \quad (63)$$

$$Dis = [Dis_1, Dis_2, \dots, Dis_n] \quad (64)$$

The next step in the FDB is to normalize the distance and the fitness as follows:

$$norm\ Dis_i = \frac{Dis_i - Dis_{min}}{Dis_{max} - Dis_{min}} \quad (65)$$

$$norm\ Obj_i = \frac{Obj_i - Obj_{min}}{Obj_{max} - Obj_{min}} \quad (66)$$

where Dis_{min} and Dis_{max} refer to the minimum and the maximum values of the distances, respectively. Obj_{min} and Obj_{max} refer to the minimum and maximum values of the objective functions. After the previous step, the score of each population will be calculated and also the score vector using Equations (67) to (69).

$$\rho = 0.5 \times \left(1 + \frac{t}{t_{max}}\right) \quad (67)$$

$$Scor_i = \rho \times (1 - norm\ Obj_i) + (1 - \rho) \times (1 - norm\ Dis_i) \quad (68)$$

$$Scor = [Scor_1, Scor_2, \dots, Scor_n] \quad (69)$$

Then, the candidate will be selected based on their scores. t_{max} is the maximum number of iterations.

4.2.2. The QOBL Method

The quasi-oppositional based learning (QOBL) is a common method employed to solve the shortage of the metaheuristic optimization techniques [70,73–79]. The concept of the QOBL is based on oppositional-based learning (OBL) which depends upon assigning the opposite point of the current solution in which it has a high probability better solution [80]. In some cases, the application of the OBL may lead to premature convergence. Thereby, quasi-oppositional-based learning can be utilized to solve this issue. The OBL of each vector can be assigned as follows:

$$X_{i,j}^* = Up_j + Lp_j - X_{i,j} \quad (70)$$

where X_j^* is the opposite vector associated with the current vector ($X_{i,j}$). Up is the upper boundary of the control variable while Lp denotes the lower value. The quasi vector refers to the center point between the upper and the lower vector and it can be represented as follows:

$$D_{i,j} = (Lp_j + Up_j) / 2 \quad (71)$$

Finally, the QOBL can be implemented to the MLCA as follows:

$$X_{i,j}^{QOBL} = \begin{cases} D_{i,j} + (X_{i,j}^* - D_{i,j}) \times rand & \text{if } (X_{i,j} < D_{i,j}) \\ D_{i,j} + (D_{i,j} - X_{i,j}^*) \times rand & \text{else} \end{cases} \quad (72)$$

4.2.3. The Chaotic Mutation

Chaos refers to a randomness and nonlinear phenomenon [81]. The aim of the chaotic mutation is to generate a set of vectors based on chaos. The logistic chaotic map is commonly implemented with the optimization method [82]. The logistic chaotic map can be described using Equation (73).

$$\vartheta(t+1) = \delta \times \vartheta(t)(1 - \vartheta(t)), \quad \vartheta(t) \in (1, 0) \quad (73)$$

where δ is the chaotic adjustment parameter that is equal to 4. The initial value $\vartheta(0) \notin \{0, 0.25, 0.5, 0.75, 1\}$.

$$X_i(t + 1) = Lp + \vartheta(t + 1)(Up - Lp); i = 1, \dots, Np \tag{74}$$

where Np is a number of the populations. The flowchart of the MLCA algorithm is shown in Figure 9.

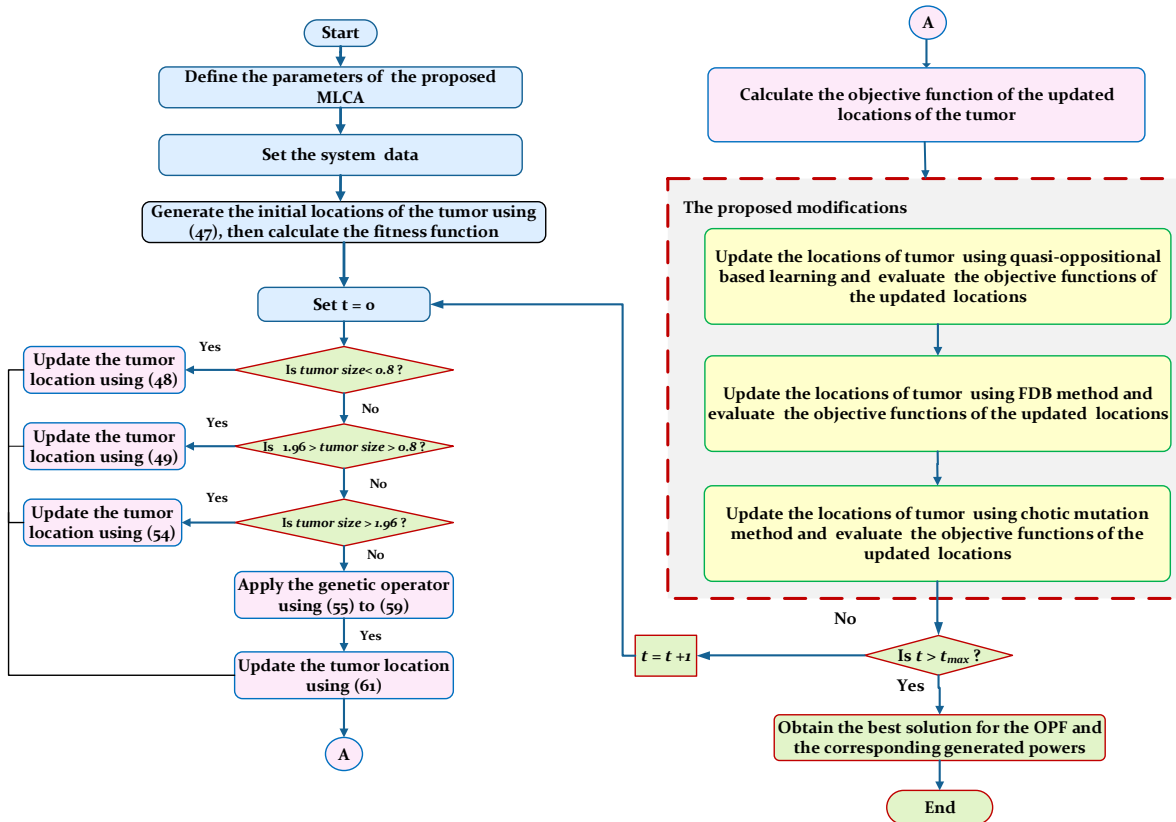


Figure 9. The flowchart of the proposed MLCA.

4.3. MLCA Verification and Results Discussion

4.3.1. Application 1: Evaluation of the MLCA in Benchmark Functions

In this section, the performance of the proposed MLCA is tested and verified in CEC 2022 benchmark functions [83]. Table 3 lists the description of the CEC 2022 benchmark functions. The obtained results by the MLCA are compared with other optimization methods including the Zebra optimization algorithm (ZOA) [84], Sand Cat swarm optimization (SCSO) [85], particle swarm optimization (PSO) [86], sine cosine algorithm (SCA) [87] and the conventional LCA. For a fair comparison, the maximum iterations and populations are selected to be 300 and 30, respectively, for all the studied algorithms and the other associated parameters are listed in Table 4.

4.3.2. Statistical Analysis

The efficacy of the MLCA is assessed through the statistical comparison with the other competitive optimization methods (SCSO, SCA, PSO, ZOA and the traditional LCA) in terms of the best, the average and the worst values of all types of CEC 2022 benchmark functions including the Unimodal, the basic, composition and hybrid benchmark functions. All statistical results were tabulated in Table 5 and the best-obtained values have been bolded. As seen in Table 5, the most competitive and superior results can be obtained by the application of the MLCA compared to SCA, SCSO, PSO, ZOA and the standard LCA. However, the PSO is the best for F5, F8 and F9 in terms of the best values.

Table 3. Description of the CEC 2022 benchmark functions.

Function	Type	Fmin	Boundaries	Description
F1	Unimodal function	300	[−100, 100]	Shifted and full rotated Zakharov function
F2		400	[−100, 100]	Shifted and full rotated Rosenbrock's function
F3	Basic functions	600	[−100, 100]	Shifted and full rotated expanded Schaffer's F6 function
F4		800	[−100, 100]	Shifted and full rotated non-continuous Rastrigin's function
F5		900	[−100, 100]	Shifted and rotated Levy function
F6	Hybrid functions	1800	[−100, 100]	Hybrid function 1 (N = 3)
F7		2000	[−100, 100]	Hybrid function 2 (N = 6)
F8		2200	[−100, 100]	Hybrid function 3 (N = 5)
F9	Composition functions	2300	[−100, 100]	Composite function 1 (N = 5)
F10		2400	[−100, 100]	Composite function 2 (N = 4)
F11		2600	[−100, 100]	Composite function 3 (N = 5)
F12		2700	[−100, 100]	Composite function 3 (N = 5)

Table 4. The selected parameters of the chosen algorithms.

Algorithm	Parameter	Value
PSO	$t_{max}, Np, C1, C2, W1$	300, 30, 2.2, 0.7
SCSC	t_{max}, Np , Sensitivity range (rg), Phases control range (R)	300, 30, [2 - 0], [−2rg, 2rg]
SCA	t_{max}, Np, b	300, 30, [2 - 0]
ZOA	t_{max}, Np, R	300, 30, 0.01
LCA	t_{max}, Np	300, 30
MLCA	t_{max}, Np, δ	300, 30, 4

Table 5. The statistical results for the competitive algorithms with the proposed MLCA.

Function No.	Optimizer	Average	Best	Worst	SD
F1	SCSO	3093.775	349.1486	8691.832	2493.022
	SCA	3458.404	1164.057	6460.631	1667.455
	PSO	300.0105	300.0001	300.1228	0.024964
	ZOA	2406.967	323.1252	7635.127	2195.524
	LCA	1447.707	700.4051	3349.518	711.4054
	MLCA	300	300	300.001	0.000205
F2	SCSO	455.7817	401.0632	720.0985	68.29365
	SCA	494.0413	432.2709	542.0408	25.87232
	PSO	424.9348	400	471.3437	30.60353
	ZOA	476.7607	404.1804	910.9457	99.36141
	LCA	420.9453	401.0094	442.2129	12.7182
	MLCA	409.3691	400	470.8066	19.38046
F3	SCSO	619.4869	603.0549	640.0254	10.06907
	SCA	625.8878	618.392	649.0927	6.258529
	PSO	620.3777	603.8081	639.1443	10.40486
	ZOA	621.8001	610.0043	633.3335	5.858331
	LCA	605.1606	601.5796	610.2001	2.407723
	MLCA	603.0268	600.2005	611.2571	3.185232
F4	SCSO	829.3113	806.1021	844.7062	8.741245
	SCA	848.0268	837.5241	860.1306	6.503605
	PSO	821.6901	809.9496	842.7831	7.669336
	ZOA	816.5859	809.1074	830.5366	5.63061
	LCA	834.6409	814.102	854.8532	10.1297
	MLCA	825.3515	804.9748	832.8336	6.299992

Table 5. Cont.

Function No.	Optimizer	Average	Best	Worst	SD
F5	SCSO	1141.826	915.4967	1469.342	171.9704
	SCA	1083.895	992.3169	1283.928	80.46401
	PSO	1054.136	900	1362.665	153.0541
	ZOA	1061.449	940.9945	1283.71	96.35584
	LCA	923.2255	901.7043	963.4934	16.85943
	MLCA	909.5508	900.6334	957.7695	12.00111
F6	SCSO	4481.64	2187.17	8161.352	1751.289
	SCA	7439635	963067.3	26425791	7135852
	PSO	3052.999	1860.679	8084.839	1582.306
	ZOA	3100.627	1881.875	7298.885	1587.5
	LCA	21954.04	2048.434	136689.1	32740.4
	MLCA	1923.427	1828.147	2521.161	141.062
F7	SCSO	2048.494	2021.093	2089.621	18.7493
	SCA	2066.766	2041.341	2085.259	10.09232
	PSO	2044.901	2012.969	2094.026	21.58967
	ZOA	2053.452	2010.803	2114.428	22.98909
	LCA	2046.143	2026.291	2066.935	11.5397
	MLCA	2025.324	2008.956	2046.95	8.875774
F8	SCSO	2227.988	2214.531	2239.62	6.081599
	SCA	2239.191	2231.123	2251.613	5.328733
	PSO	2235.924	2200.537	2341.024	39.94917
	ZOA	2231.259	2222.731	2352.093	25.27378
	LCA	2229.289	2222.178	2231.57	2.287831
	MLCA	2219.969	2203.455	2224.124	4.350484
F9	SCSO	2594.81	2529.458	2678.021	35.10836
	SCA	2598.177	2557.816	2656.696	27.8627
	PSO	2541.842	2529.284	2676.216	40.64008
	ZOA	2614.066	2530.239	2718.711	45.68827
	LCA	2539.873	2531.308	2556.745	6.301353
	MLCA	2529.411	2529.284	2531.277	0.397224
F10	SCSO	2530.18	2500.426	2635.02	53.1725
	SCA	2528.239	2501.45	2673.45	58.37221
	PSO	2596.806	2500.387	2759.12	68.34379
	ZOA	2578.921	2500.553	2681.633	71.62236
	LCA	2500.802	2500.463	2501.487	0.222178
	MLCA	2500.435	2500.276	2500.703	0.1111
F11	SCSO	2831.009	2609.066	3309.952	170.1567
	SCA	3004.421	2793.088	3783.863	297.7186
	PSO	2953.419	2600.001	5230.808	485.1794
	ZOA	3053.657	2745.179	3430.171	182.3106
	LCA	2731.127	2636.21	2764.63	34.56173
	MLCA	2624.072	2600	2750.473	56.29244
F12	SCSO	2874.063	2861.454	2918.708	16.46731
	SCA	2873.296	2867.157	2891.819	4.697798
	PSO	2951.277	2872.847	3121.534	69.80949
	ZOA	2943.05	2895.543	3012.8	31.04917
	LCA	2869.805	2865.583	2875.687	2.388877
	MLCA	2871.416	2864.046	2898.943	7.599243

4.3.3. Convergence Analysis

The convergence plotting can also be utilized to assess the performance of the suggested MLCA. Figure 10 shows the convergence plots of the MLCA with respect to SCA, SCSO, PSO, ZOA and the standard LCA. For the Unimodal (F1), the suggested MLCA is converged at 123th which is the best, compared to the other methods, in terms of the

convergence speed and the accuracy. Likewise, for the basic, composition, and hybrid benchmark functions, the suggested optimizer converged rapidly before the 150th iteration except for F8; the PSO is the best.

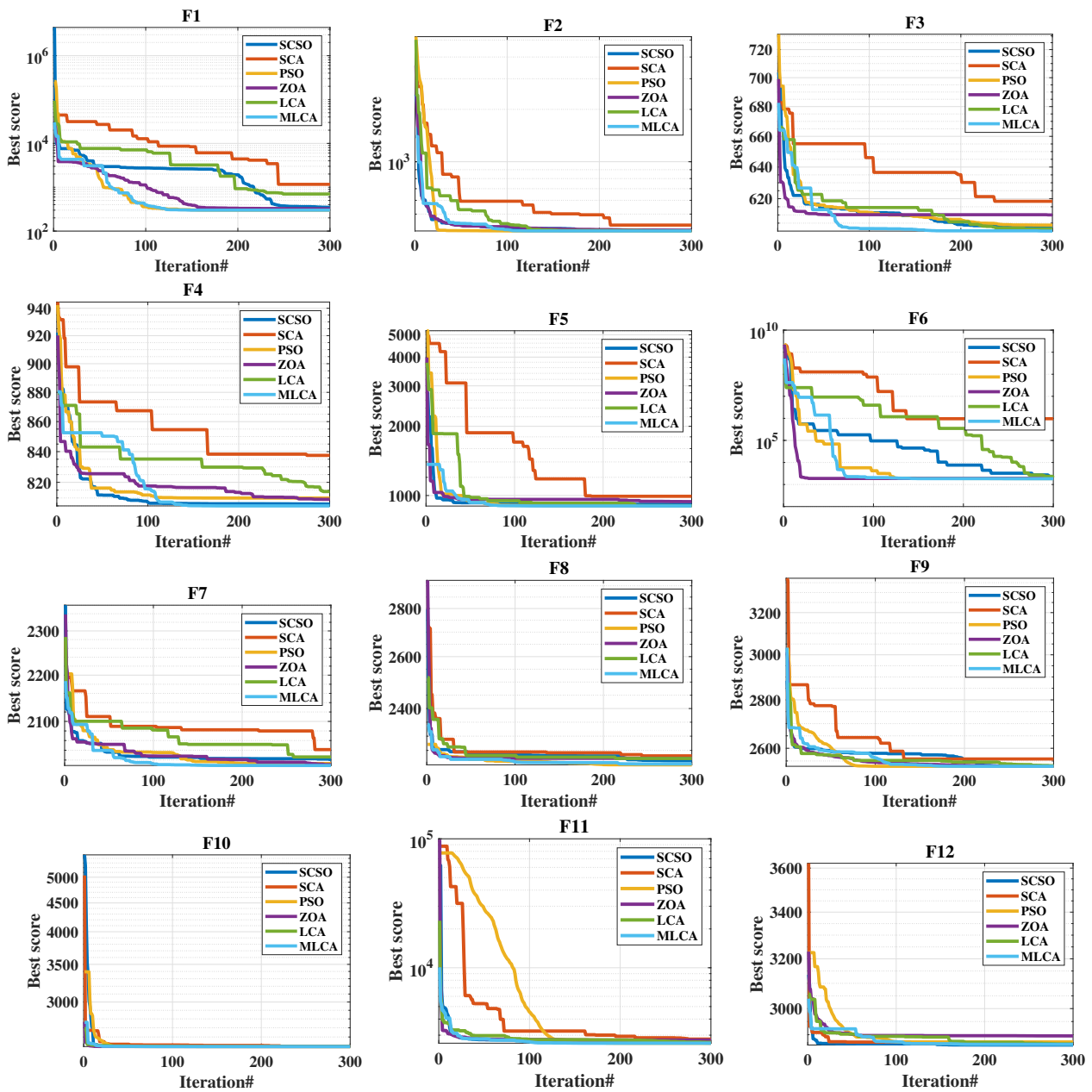


Figure 10. The convergence plots of the MLCA and the competitive techniques.

4.3.4. Boxplot Analysis

The boxplot is the third method that can be used for assessing the performance and efficacy of the MLCA with competitive techniques. The boxplot can provide the visual distribution of the obtained data from the reported optimizers. Figure 11 lists the boxplot for all objective functions by SCA, SCSO, PSO, ZOA standard LCA and the proposed MLCA. Judging from Figure 11, the suggested MLCA has the narrowest boxplot and interquartile range; its median is the lowest compared to other optimizers, which verifies that the MCLA is the best and superior compared to other algorithms.

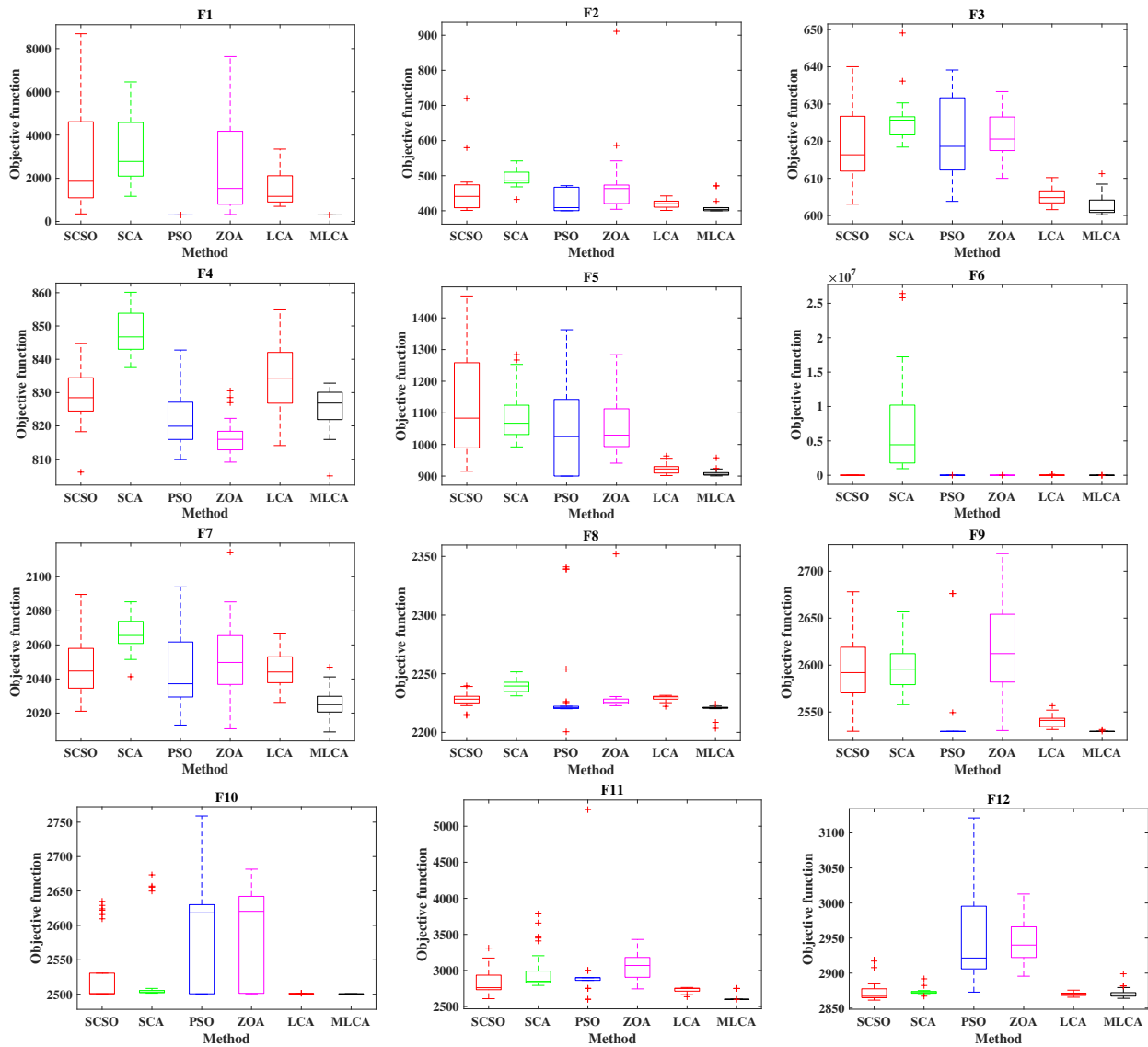


Figure 11. The boxplot of the MLCA and the competitive techniques.

4.3.5. Wilcoxon and Fredman Tests

The Wilcoxon test is a robust statistical tool that is used to compare two data that are not normally distributed [88]. The p -value of the Wilcoxon test is the most important value that can describe if there is a high difference between the results or not. When the p -value is less than 0.05, this means that there is a meaningful difference, while when this value is more than 0.05 this means that there is no significant difference between the results. Table 6 shows the p -values of the proposed MLCA compared with SCSO, PSO, SCA, and the standard LCA. According to the outcomes of Table 6, most of the values are less than 0.05, which means that there are significant differences between the obtained results and between the studied optimization methods, except there is no significant difference between MLCA and SCSO for F12 and also between MLCA and PSO for F2 and F7. Likewise, there is no notable difference between MLCA and LCA for F12.

The Fredman test is a statistical tool that can be used to compare the results of multiple optimization methods and illustrates if there is a notable difference in the mean ranks of the optimizers' outcomes [89]. Figure 4 shows the results of the Fredman test of MLCA, LCA, SCSO, SCA, PSO, and ZOA. Judging from Figure 4, the ranking of the MLCA, LCA, SCSO, SCA, PSO, and ZOA based on the mean rank values are 1, 2, 4, 6, 3 and 5,

respectively. It is clear that the MCLA is a robust and superior technique compared to other optimization methods.

Table 6. The p -values of Wilcoxon's rank sum test for the MLCA with the other optimization methods.

MLCA vs.	SCSO	SCA	PSO	FOX	LCA
F1	1.4157×10^{-9}	1.4157×10^{-9}	5.2120×10^{-9}	1.4157×10^{-9}	1.4157×10^{-9}
F2	9.6957×10^{-6}	3.6690×10^{-9}	1.1159×10^{-1}	3.3440×10^{-7}	8.1897×10^{-5}
F3	9.2880×10^{-9}	1.4157×10^{-9}	1.3079×10^{-8}	1.5967×10^{-9}	1.6708×10^{-3}
F4	8.7677×10^{-2}	1.4055×10^{-9}	1.8376×10^{-2}	2.1373×10^{-5}	9.6989×10^{-4}
F5	2.2857×10^{-9}	1.4157×10^{-9}	2.9771×10^{-2}	1.8002×10^{-9}	3.3128×10^{-4}
F6	2.5742×10^{-9}	1.4157×10^{-9}	3.2928×10^{-5}	2.6597×10^{-6}	2.0288×10^{-9}
F7	1.6471×10^{-6}	1.5967×10^{-9}	1.1285×10^{-4}	6.7951×10^{-7}	1.0585×10^{-7}
F8	3.7045×10^{-7}	1.4157×10^{-9}	8.0086×10^{-1}	1.8002×10^{-9}	2.0288×10^{-9}
F9	1.8002×10^{-9}	1.4157×10^{-9}	1.5288×10^{-6}	1.5967×10^{-9}	1.4157×10^{-9}
F10	2.5677×10^{-8}	1.4157×10^{-9}	2.4184×10^{-6}	2.0288×10^{-9}	1.6401×10^{-8}
F11	1.3090×10^{-7}	1.4157×10^{-9}	8.2805×10^{-9}	2.2857×10^{-9}	3.0175×10^{-7}
F12	1.8064×10^{-1}	3.3915×10^{-3}	1.0414×10^{-8}	1.5967×10^{-9}	5.7365×10^{-1}

The Friedman test is a statistical tool that can be used to compare the results of multiple optimization methods and illustrates if there is a notable difference in the mean ranks of the optimizers' outcomes [89]. Figure 12 shows the results of the Friedman test of MLCA, LCA, SCSO, SCA, PSO, and ZOA. Judging from Figure 12, the ranking of the MLCA, LCA, SCSO, SCA, PSO, and ZOA based on the mean rank values are 1, 2, 4, 6, 3 and 5, respectively. It is clear that the MCLA is a robust and superior technique compared to other optimization methods.

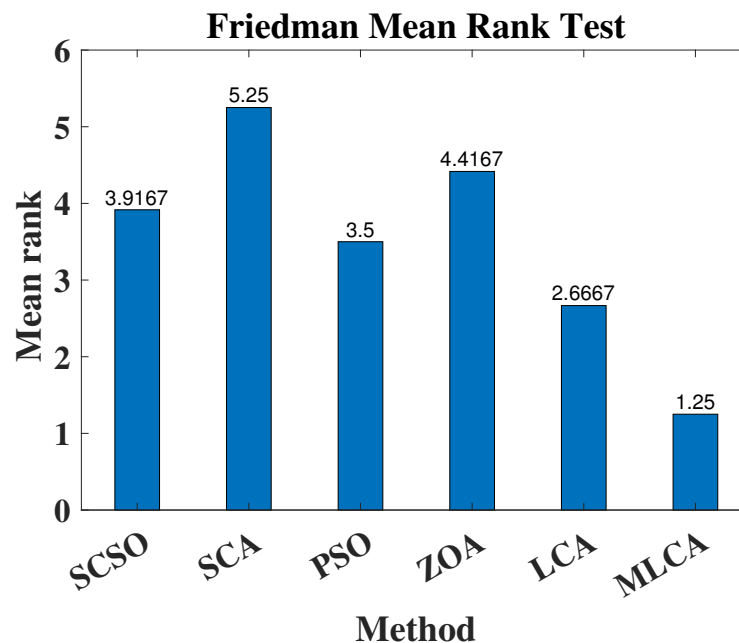


Figure 12. Friedman's rank test of the MLCA with the competitive optimizers.

4.4. The Proposed MLCA-Based Control Parameters Optimization Process

The proposed 1+TD/FOTIDF LFC possesses nine parameters in the MG area a (K_{t1} , K_{d1} , n_1 , K_{t2} , n_2 , K_{i1} , λ_1 , K_{d2} , and N_{c2}). Also, the MG area b has another nine parameters (K_{t3} , K_{d3} , n_3 , K_{t4} , n_4 , K_{i2} , λ_2 , K_{d4} , and N_{c2}). A total of 18 tunable design parameters in the proposed 1+TD/FOTIDF LFC method is summarized in Table 7. The proposed MLCA

is employed for determining optimum values for the 18 parameters simultaneously for obtaining the best performance and disturbance rejections. The main directing factor for the optimization algorithm is the selected objective function of the process. The main four objectives for LFC design are integral-squared errors (ISE), integral-absolute errors (IAE), integral-time-squared errors (ITSE), and integral-time-absolute errors (ITAE). Their general representations are as follows:

$$\begin{aligned}
 ISE &= \int \sum_{i=1}^m (e_i^2) dt \\
 IAE &= \int \sum_{i=1}^m abs(e_i) dt \\
 ITSE &= \int \sum_{i=1}^m (e_i^2) t.dt \\
 ITAE &= \int \sum_{i=1}^m abs(e_i) t.dt
 \end{aligned}
 \tag{75}$$

Table 7. The optimum parameters using MLCA optimizer.

Controller	Area	Parameters										
		K_{t1}	K_{i1}	K_{d1}	n_1	K_{t2}	K_{i2}	K_{d2}	n_2	λ_1	μ_1	N_{f1}
FOTID	<i>a</i>	2.245	1.987	1.713	2.234	—	—	—	—	0.622	0.574	—
	<i>b</i>	2.956	2.016	0.895	2.923	—	—	—	—	0.714	0.882	—
TI/FOTID	<i>a</i>	3.155	2.019	—	2.862	2.868	3.036	1.156	3.634	0.882	0.857	—
	<i>b</i>	2.738	1.583	—	3.235	2.365	2.678	1.344	3.69	0.566	0.843	—
TD/FOTID	<i>a</i>	3.928	—	1.037	3.555	4.018	3.346	2.147	3.944	0.788	0.948	—
	<i>b</i>	3.748	—	1.164	4.022	3.571	3.176	2.291	3.891	0.758	0.788	—
1+TD/FOTIDF	<i>a</i>	4.525	—	3.851	4.576	4.864	3.865	3.998	4.977	0.948	0.877	151.36
	<i>b</i>	4.118	—	4.073	4.281	3.954	4.279	3.092	4.583	0.882	0.915	189.5

The directing objective function for interconnected MGs includes the minimization of frequency deviations in each connected area (in the studied case, minimizing Δf_a and Δf_b). Additionally, the minimization of tie-line power deviations between connected areas (in the studied case minimizing (ΔP_{tie})). The three objectives in the studied case include Δf_a , Δf_b , and (ΔP_{tie}) . They are combined in a single objective function. Using definitions of ISE, IAE, ITSE, and ITAE objectives in Equation (75), the objective functions can be formulated as:

$$\begin{aligned}
 ISE &= \int_0^{t_s} ((\Delta f_a)^2 + (\Delta f_b)^2 + (\Delta P_{tie})^2) dt \\
 IAE &= \int_0^{t_s} (abs(\Delta f_a) + abs(\Delta f_b) + abs(\Delta P_{tie})) dt \\
 ITSE &= \int_0^{t_s} ((\Delta f_a)^2 + (\Delta f_b)^2 + (\Delta P_{tie})^2) t.dt \\
 ITAE &= \int_0^{t_s} (abs(\Delta f_a) + abs(\Delta f_b) + abs(\Delta P_{tie})) t.dt
 \end{aligned}
 \tag{76}$$

The process of parameter optimization is constrained by the following ranges for each tunable parameter:

$$\begin{aligned}
 K_t^{min} &\leq K_{t1}, K_{t2} \leq K_t^{max} \\
 K_i^{min} &\leq K_{i1}, K_{i2} \leq K_i^{max} \\
 K_d^{min} &\leq K_{d1}, K_{d2} \leq K_d^{max} \\
 \lambda^{min} &\leq \lambda_1, \lambda_2 \leq \lambda^{max} \\
 \mu &\leq \mu_1, \mu_2 \leq \mu^{max} \\
 N_c &\leq N_{c1}, N_{c2} \leq N_c^{max}
 \end{aligned}
 \tag{77}$$

In which, $(f)^{max}$ and $(f)^{min}$ are referred to upper, and lower constraints, respectively, for tunable parameters. Lower limiting constraints for $(K_t^{min}, K_i^{min}, K_d^{min})$ are selected at zero, and upper ones $(K_t^{max}, K_i^{max}, K_d^{max})$ are selected at 5 in the proposed process. FO operator λ possesses a lower value λ^{min} at 0 and its upper one λ^{max} is selected at 1. The tilt operator n is set in the range [2–10] and N_c is set in the range [5–300]. Figure 13 shows the proposed MLCA-based parameters optimization method.

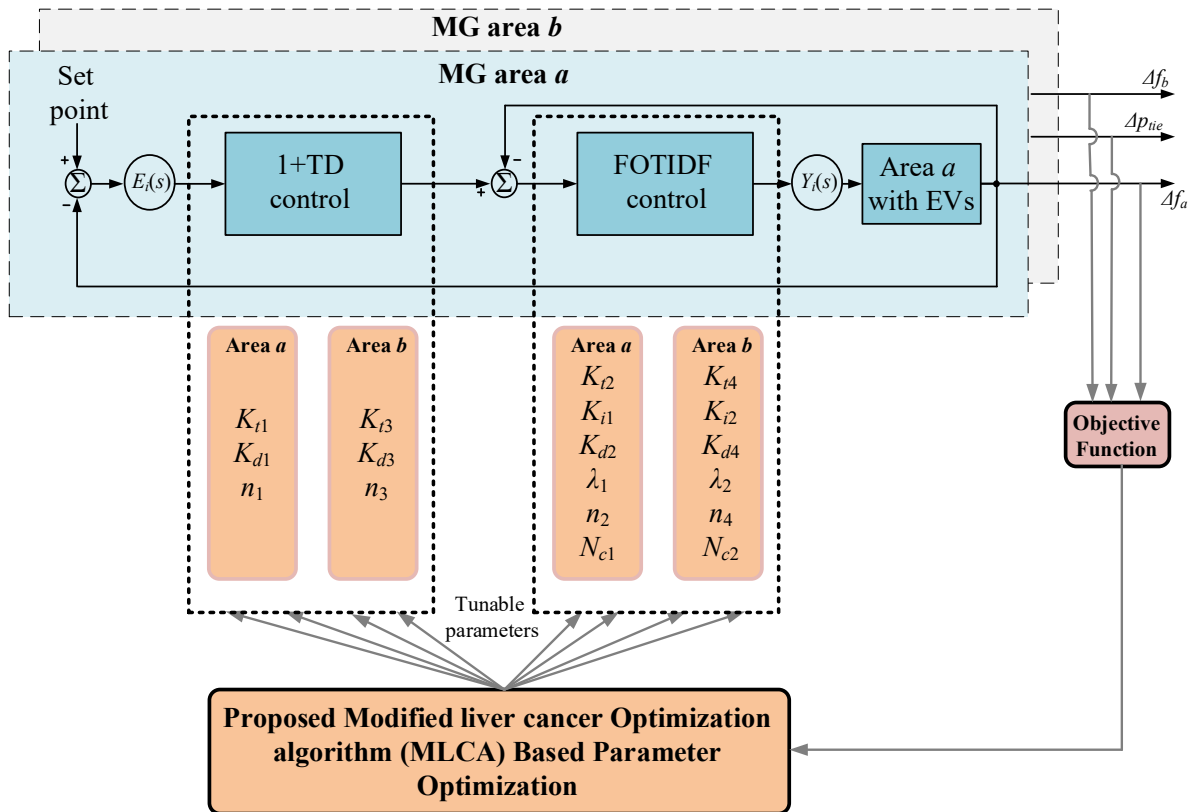


Figure 13. Proposed MLCA based parameters optimization method.

5. Results and Discussions

The programming code for tuning the proposed CC 1+TD/FOTIDF controller based-MLCA algorithm has been implemented using a MATLAB m-file via a personal computer with an Intel®i7 1.9 GHz processor and 12 GB RAM (HP, iyadh, Saudi Arabia). This code is interfaced with the Simulink model of the dual area MG power system to execute the optimization process with a twenty populations number and one hundred iterations to tune the parameters of the suggested CC 1+TD/FOTIDF, TD/FOTID, TI/FOTID, and FOTID controllers. Furthermore, the convergence performance of the MLCA code is examined and compared with the other algorithms, such as SCA, SCSO, PSO, ZOA, and LCA, as shown in Figure 10, which proves that the MLCA technique has a faster convergence rate with a smoother curve compared to meta historical methods. To approve the proposed scheme validation and the investigated algorithm, the dual area MG power system has been conducted under identical operating scenarios such as step load change (SLC) and different cases of PV irradiation conditions and wind speed variations. In these scenarios, the stability and frequency variation responses of the proposed control technique are compared to those of conventional and fractional controllers to evaluate its superiority. It should be noted that the scenarios of PV penetration are based on real solar radiation data. The measurements of global solar radiation were acquired from the King Abdullah City for Atomic and Renewable Energy (KACARE), the primary authorized organization responsible for gathering and overseeing data on renewable energy resources in Saudi Arabia. These scenarios are organized as follows:

5.1. Scenario 1: 2% Step Load Change (SLC)

The proposed CC 1+TD/FOTIDF controller based on the MLCA is investigated by employing 2% SLC at time $t = 75$ s in area a without using RESs in the studied dual area microgrid system considering the GRC. Figure 14 presents the waveforms of change rate in interconnected line power and system frequency in the dual areas a and b for the studied multi-area power network. This scenario tests the various control patterns such as FOTID, TI/FOTID, TD/FOTID, and proposed CC controllers based on the MLCA for simulation intention via the influence of a 2% SLP. It is spotted from this figure that the MLCA-based CC 1+TD/FOTIDF control, with the percentage participation of the EV, offers remarkable performance with an amazing decrease in frequency and power deviations compared to other traditional and fractional control structures. The value of the frequency deviation of the investigated MG network with the FOTID controller has been maintained at 0.0115 Hz for area a and 0.0082 Hz for area b , with an interconnected-line power deviation within 0.0028 p.u in this status. According to the TI/FOTID, the system frequency has been kept to 0.0079 Hz for area a and 0.0058 Hz for area b and the perversion of interconnected-line power is 0.0024 p.u during the perturbation of a 2% load change at 75 s instant. However, the results obtained from the TD/FOTID controller were acceptable regarding the previous two controllers. In contrast, the tie-line power is 0.0016 p.u and the frequency reached 0.0058 Hz for area a and 0.0023 Hz for area b . Conversely, the CC 1+TD/FOTID has a strong performance by reducing the network frequency variation of the investigated dual area MG system to 0.0001 Hz for area a and 0.0005 Hz for area b while maintaining the power deviation at 0.00008 p.u. The numerical estimations of the examined MG system's dynamic restraint in terms of maximum and minimum overshoots and settling time for step load adjustment are summarized in Table 8. When compared to other controllers, the CC 1+TD/FOTID controller, which is based on the MLCA, performs exceptionally well. From another side, Figure 15 shows that the MG system is simulated without considering the GRC limits at the same operation. It can be observed that not utilizing the GRC results in a lower peak undershoot and a smaller settling time for all the suggested controllers. Furthermore, the performance of the proposed controller with and without the GRC limits is depicted in Figure 16, which indicates the deterioration of the system's dynamic performance. Therefore, a GRC limit must be included for the realistic study of the MG system.

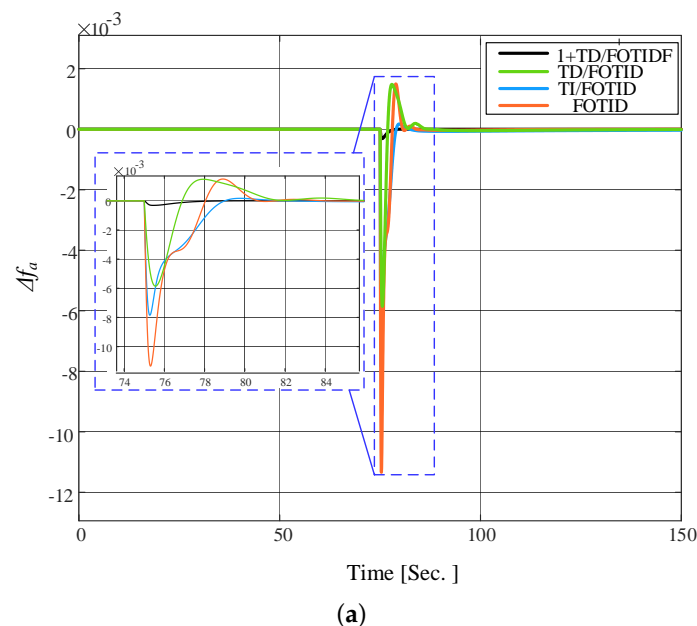


Figure 14. Cont.

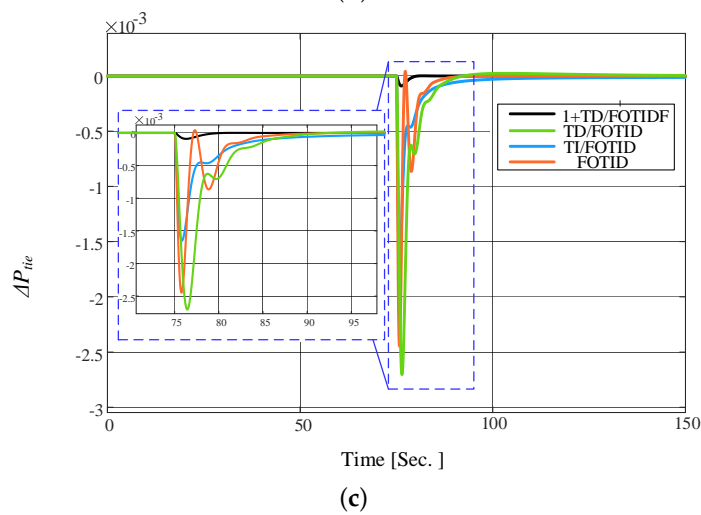
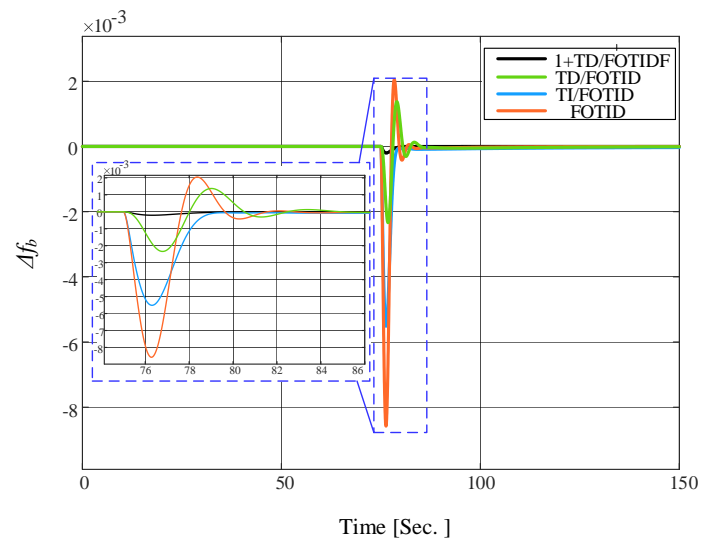


Figure 14. Performance results at Scenario 1 with GRC. (a) Δf_a (P.U); (b) Δf_b (P.U); (c) ΔP_{tie} (P.U).

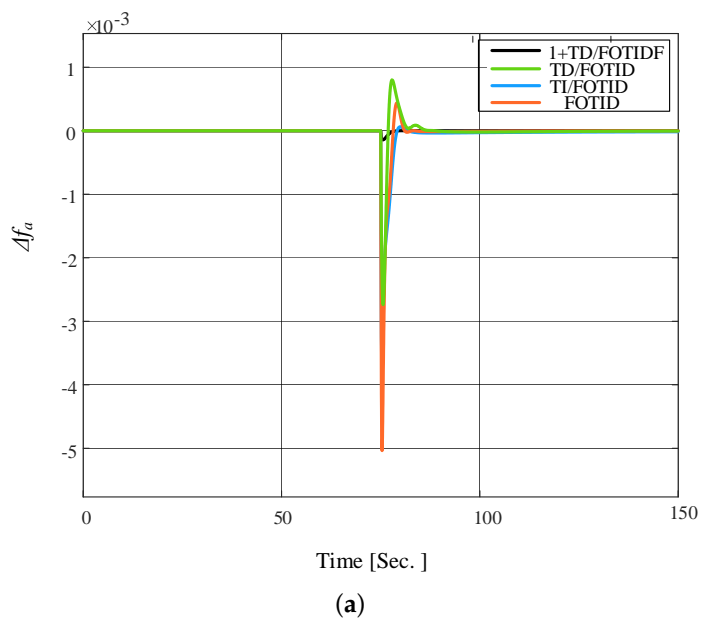
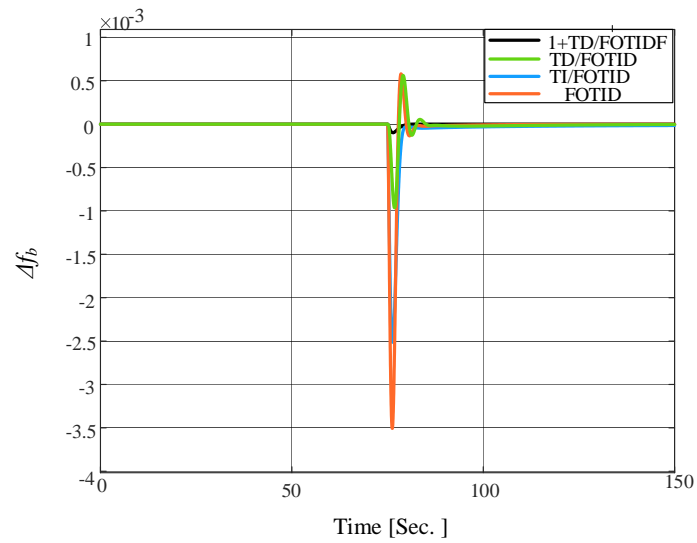
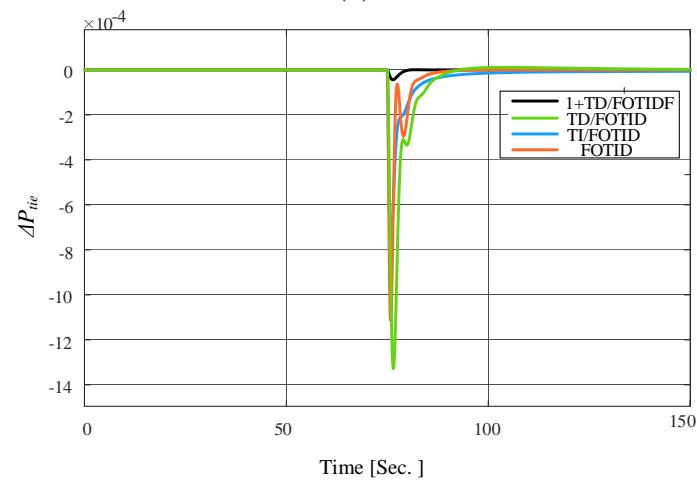


Figure 15. Cont.



(b)



(c)

Figure 15. Performance results at Scenario 1 without GRC. (a) Δf_a (P.U.); (b) Δf_b (P.U.); (c) ΔP_{tie} (P.U).

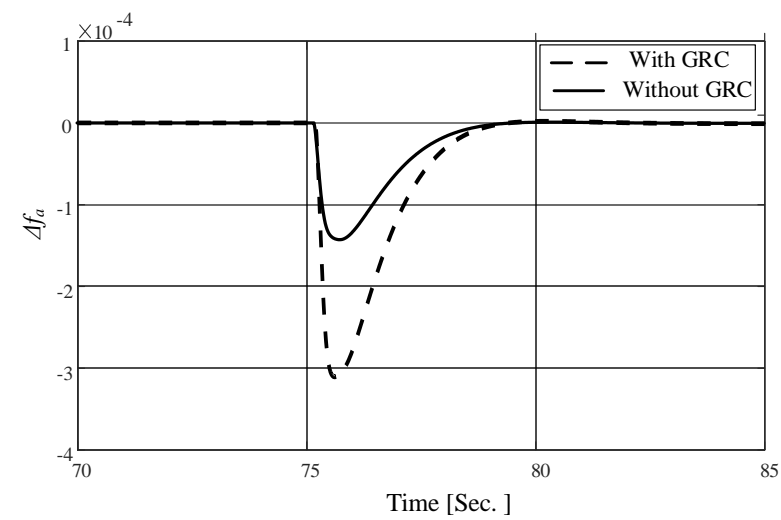


Figure 16. Frequency response Δf_a (P.U) with and without GRC of the proposed controller.

Table 8. The obtained results for the tested scenarios.

Scenario	Controller	Δf_1 (P.U)			Δf_2 (P.U)			ΔP_{tie} (P.U)		
		PO	PU	ST (s)	PO	PU	ST (s)	PO	PU	ST (s)
No.1 at 75 s	FOTID	0.0019	0.0115	17	0.0021	0.0082	16	0.0005	0.0028	22
	TI/FOTID	0.0002	0.0079	9	0.0016	0.0058	20	0.0001	0.0024	18
	TD/FOTID	0.0017	0.0058	15	0.0001	0.0023	10	0.0002	0.0016	10
	1+TD/FOTIDF	-	0.0001	4	-	0.0005	5	-	8.4×10^{-5}	6
No.2 at 8:00 AM.	FOTID	0.0016	0.0012	FU	0.0017	0.0011	FU	0.0004	0.0005	FU
	TI/FOTID	0.0017	0.0018	FU	0.0019	0.0015	FU	0.0006	0.0007	FU
	TD/FOTID	0.0008	0.0009	FU	0.0005	0.0007	FU	0.0007	0.0009	FU
	1+TD/FOTIDF	1×10^{-6}	1×10^{-5}	FU	1.1×10^{-6}	1.01×10^{-5}	FU	1×10^{-6}	1.1×10^{-6}	FU
No.3 at 13:00 PM.	FOTID	0.0012	0.0042	FU	0.0025	0.0073	FU	0.0016	0.0004	FU
	TI/FOTID	0.0011	0.0023	FU	0.0019	0.0041	FU	0.0011	0.0003	FU
	TD/FOTID	0.0001	0.0021	FU	0.0014	0.0037	FU	0.0009	0.0001	FU
	1+TD/FOTIDF	1×10^{-5}	1×10^{-5}	FU	0.9×10^{-5}	1×10^{-6}	FU	1×10^{-4}	1×10^{-6}	FU
No.4 at 10:00 AM.	FOTID	0.0057	0.0099	FU	0.0072	0.0133	FU	0.0039	0.0021	FU
	TI/FOTID	0.0028	0.0058	FU	0.0041	0.0033	FU	0.0022	0.0013	FU
	TD/FOTID	0.002	0.004	FU	0.0036	0.0031	FU	0.0021	0.0011	FU
	1+TD/FOTIDF	0.0001	0.0004	FU	0.0001	0.0001	FU	1×10^{-4}	1×10^{-5}	FU
No.5 at 16:00 PM.	FOTID	0.141	0.022	FU	0.123	0.0392	FU	0.033	0.0067	FU
	TI/FOTID	0.0826	0.0018	FU	0.0524	0.0141	FU	0.0192	0.0031	FU
	TD/FOTID	0.0522	0.0151	FU	0.0198	0.011	FU	0.022	0.0023	FU
	1+TD/FOTIDF	0.004	-	120	0.001	-	110	0.0013	-	180

FU = Fluctuated.

5.2. Scenario 2: SLC with PV Irradiation Case A

At the same load profiles of the previous scenario, a 24 h practical PV profile is integrated at area *b*, in this case, to examine the performance of the suggested CC 1+TD/FOTID, FOTID, TI/FOTID, and TD/FOTID control structures under the variation conditions of solar units. The PV irradiance, temperature, and power profiles are shown in Figure 17 for this scenario. Figure 18 and Table 8 show the control response results of this case. This table proves that the CC proposed controller has the ability to obtain the lowest value of frequency deviation compared to the FOTID controller, the TI/FOTID controller, and the TD/FOTID controller. Furthermore, it has the best damping characteristics in frequency and tie-line power deviations at SLC and during increasing and decreasing periods of PV power compared to other characteristics from other controllers as shown in Figure 18. Conversely, the control signal provided by the planned CC 1+TD/FOTID controller achieved faster EV performance, high EV discharge and less power consumption from the traditional thermal and hydraulic units than the other controllers. As a result, it is clear from this illustration that the new MLCA technique-based suggested that the CC 1+TD/FOTID controller is the most reliable one in that particular LFC scenario.

5.3. Scenario 3: SLC with PV Irradiation Case B

For the validation of the proposed CC 1+TD/FOTID controller, which is fine-tuned by the MLCA technique, the simulation experiments of this scenario have been accomplished under the two SLCs in both areas for 2%, besides a severe cloudy condition of the PV power generation which is attained from the incoming irradiance and temperature profiles for 24 h in Figure 19. This PV profile has a severe drop in its power value at $t = 1:00$ PM, which reflects the robustness and efficacy of the proposed CC controller. Figure 20 shows a contrast effect of the investigated controllers in terms of frequency and power deviations of the dual area MG system. It is noteworthy that the proposed controller displays greater

genealogical stability than the other techniques of control. This figure implies that the aberration of the frequency with the CC 1+TD/FOTID controller is less than ± 0.00005 Hz at the initial time of simulation and less than ± 0.00002 Hz at the instant of the cloudy period, which causes a significant power drop of PV units. While the deviation with FOTID, TI/FOTID, and TD/FOTID arrives at ± 0.012 Hz, ± 0.009 Hz and 0.005 Hz at $t = 0$ s, respectively, and at ± 0.004 Hz, ± 0.003 Hz and 0.002 Hz at cloudy times, respectively, in area *a*. Furthermore, the effectiveness of the new CC controller can be noted in Figure 21, which proves that the required power from thermal generation during load and PV variations using the CC 1+TD/FOTID is smaller than with the other controllers, and that specifies the role of the proposed technique. In addition, the different performance effect of the four controllers on the EV action is depicted in Figure 21. It indicates that the proposed method presents a large and fast charge/discharge process compared with the other three techniques. Therefore, these results prove that the inner loop of the proposed CC controller responds instantly to the dynamics initiated by PV power and other generation sources in the dual area system, as well as the outer control loop, which can handle the load perturbations and system dynamics.

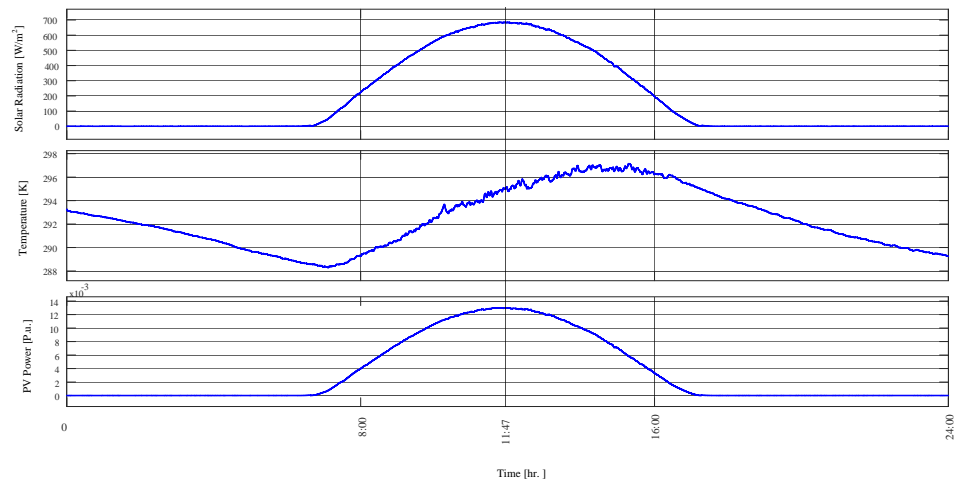


Figure 17. PV generation characteristics of scenario 2.

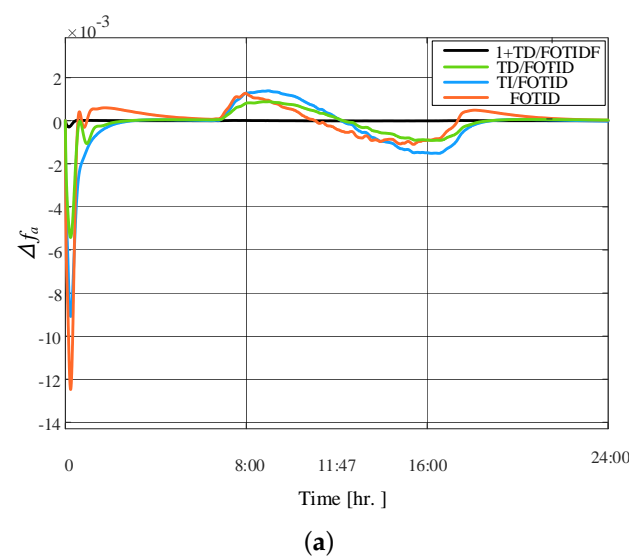
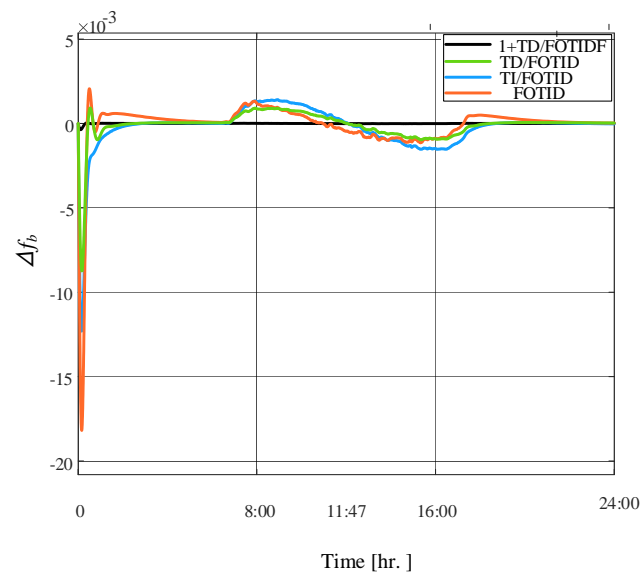
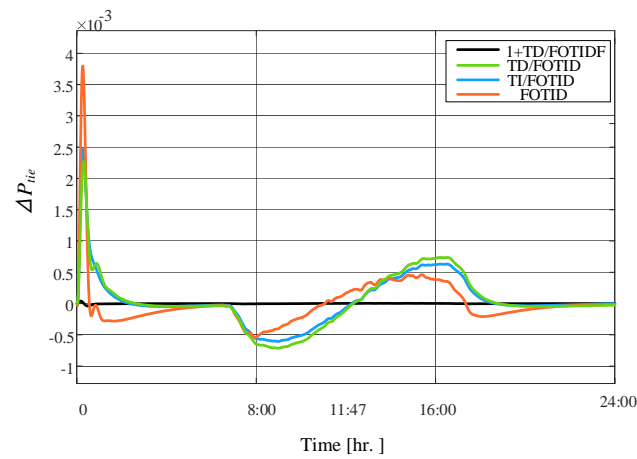


Figure 18. Cont.



(b)



(c)

Figure 18. Performance results at Scenario 2. (a) Δf_a (P.U); (b) Δf_b (P.U); (c) ΔP_{tie} (P.U).

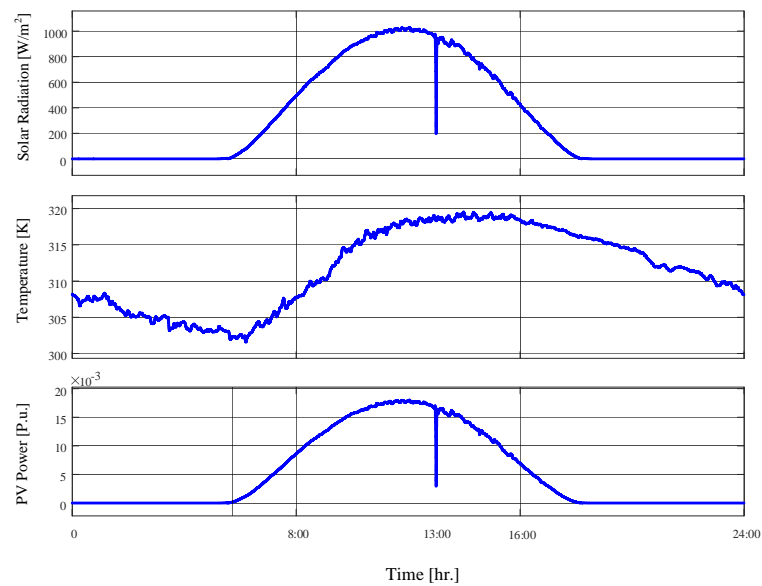


Figure 19. PV generation characteristics of scenario 3.

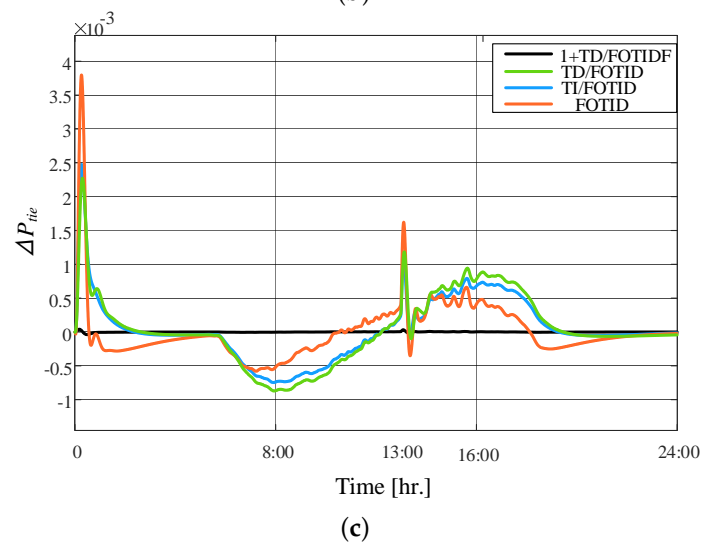
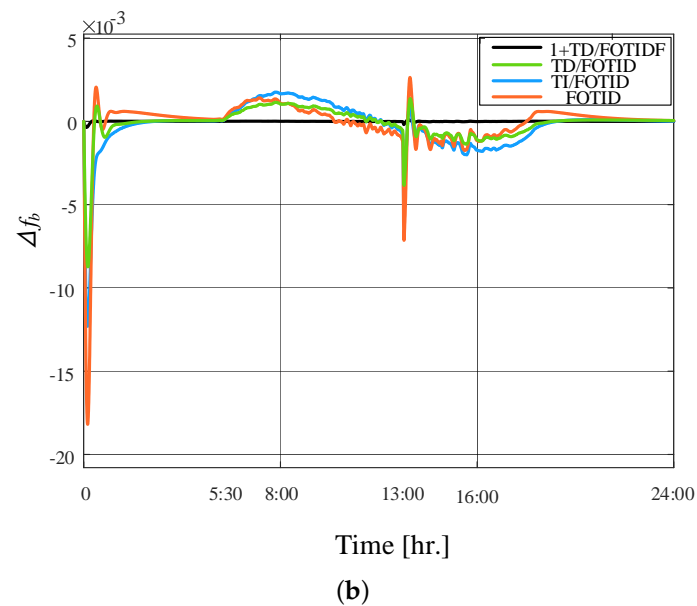
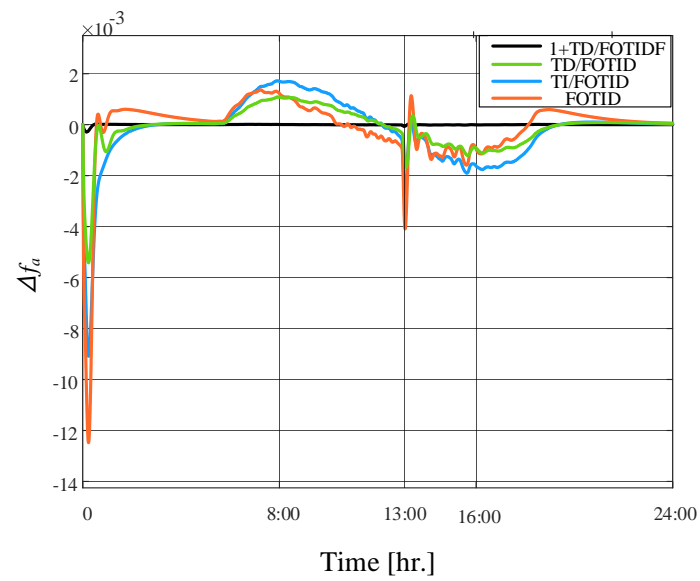


Figure 20. Performance results at Scenario 3. (a) Δf_a (P.U.); (b) Δf_b (P.U.); (c) ΔP_{tie} (P.U.).

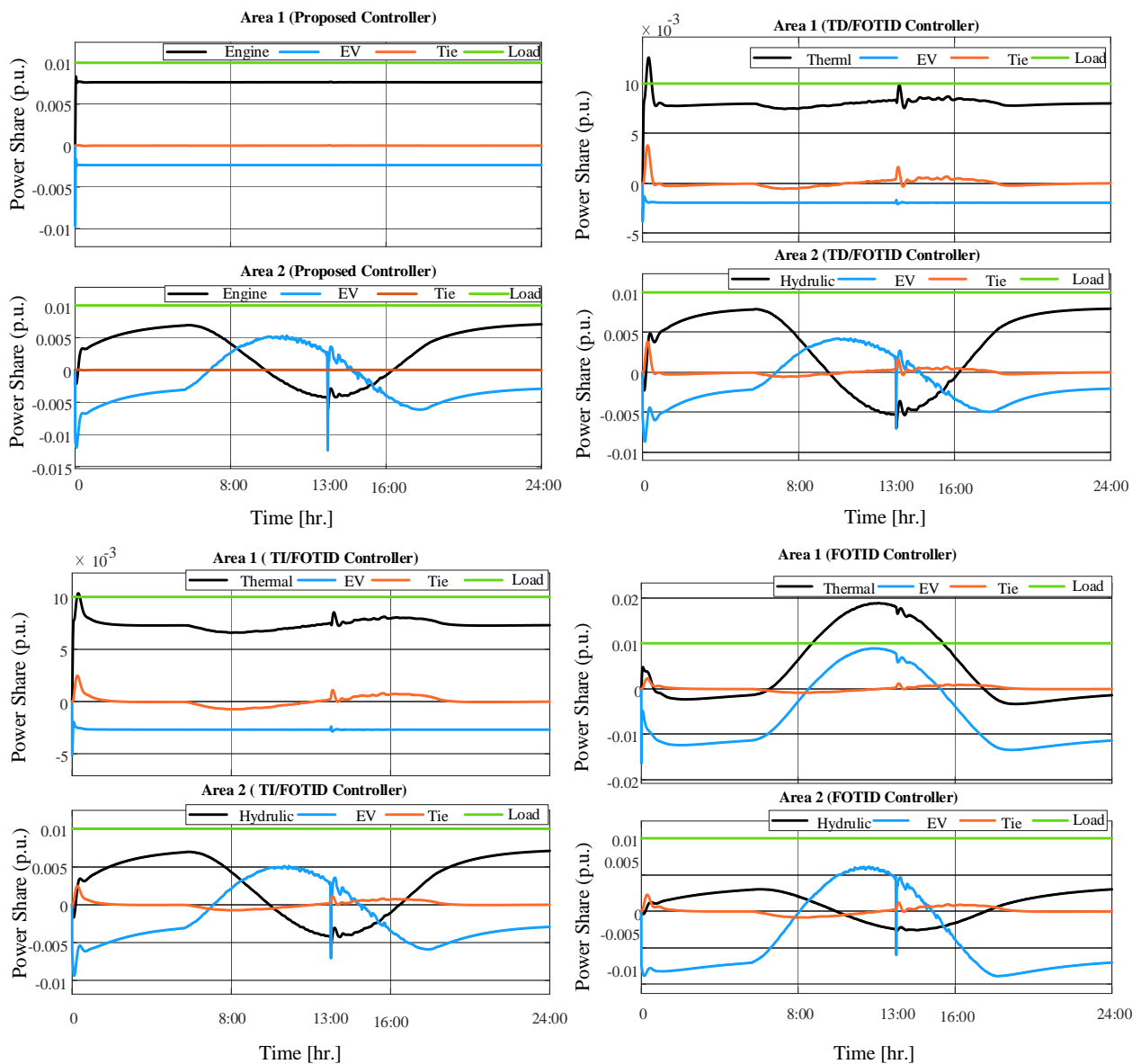


Figure 21. Performance of generators and EVs at Scenario 3.

5.4. Scenario 4: SLC with sever PV Irradiation Case C

The capability of the suggested CC 1+TD/FOTID LFC coordinated with EVs based on the MLCA technique is assessed and demonstrated under an extreme disturbance condition from the PV units. Solar power has a very bad irradiation output, which causes severe power oscillations in this case, as depicted in Figure 22. Therefore, this scenario became a great challenge facing the suggested LFC techniques. Figure 23 shows the acquired frequency and interconnected-line power variations of the investigated dual area microgrid system for this situation. It can be observed that the CC 1+TD/FOTID control comes first in reducing the frequency and power aberrations in contrast to alternative control methods. It can dampen the system frequency oscillations smoothly within 0.0004 Hz for area *a* and 0.0001 Hz for area *b* and maintain tie-power change within 0.0001 p.u. during severe periods of PV irradiance fluctuations at 10 AM. The TD/FOTID came in the second order with frequency deviating at 0.004 Hz for area *a*, 0.0031 Hz for area *b*, and ± 0.0011 p.u. for grid frequencies and interconnected-line power, respectively. TI/FOTID comes thirdly by upholding the frequency deviancy at 0.0058 Hz for area *a* and 0.0033 Hz for area *b* and keeping tie-line power value within 0.0013 P.U. While the FOTID controller comes last, it has the highest overshoot and undershoot in frequency diffraction within 0.0099 Hz for area

a and 0.0133 Hz for area b and keeps tie-line power change within 0.0021 p.u compared to the proposed one and other traditional tie controllers. From another side, Figure 24 shows the feature of the dual loops of the CC 1+TD/FOTIDF technique in controlling the discharge from the EV and required power from thermal and hydraulic generators with respect to other control methods.

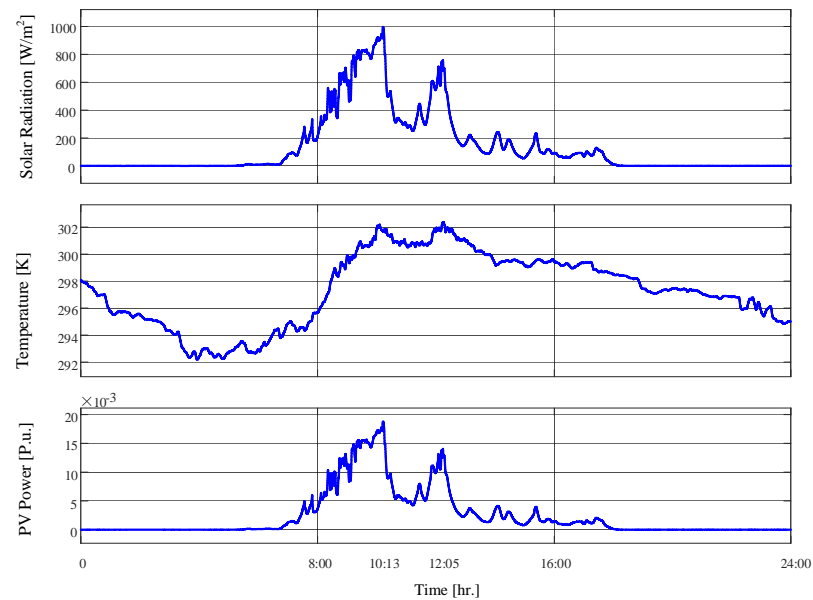
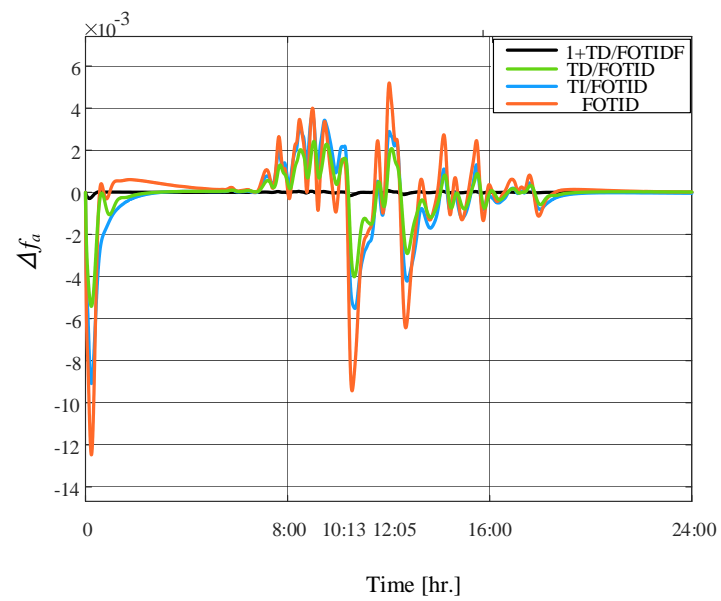


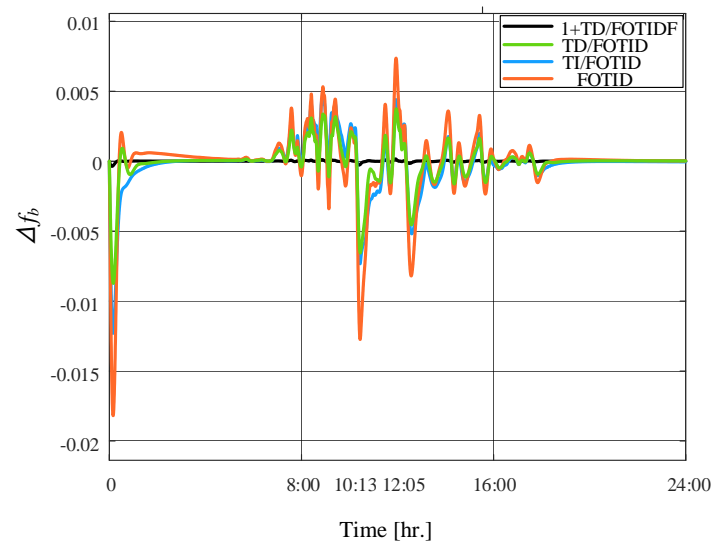
Figure 22. PV generation characteristics of scenario 4.

5.5. Scenario 5: High RESs of PV and Wind Generation

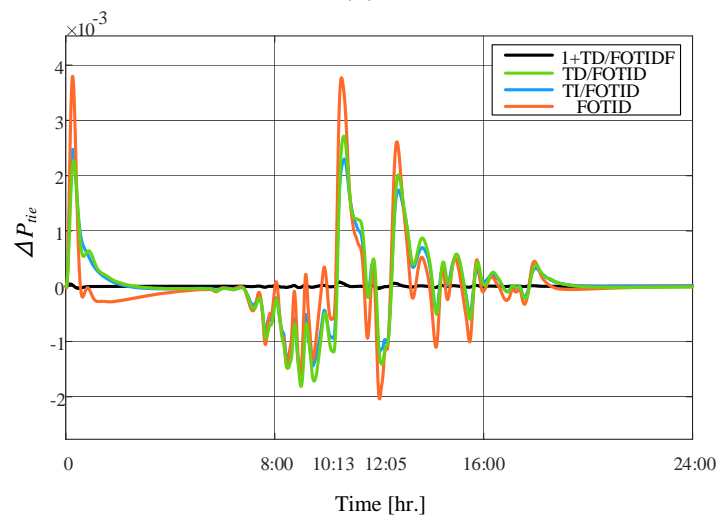
In this case, the electric generation of the dual area MG is increased by adding a wind generation farm. Its profile is shown in Figure 25. However, a power imbalance in the MG system can occur due to the uncertainty in the wind speed which in turn causes severe frequency and power fluctuations. Therefore, this scenario takes into consideration the highly fluctuating wind power besides the integration of PV power and load change impacts of scenario 2 on the investigated power grid. The contrast performance of the four suggested controllers on the studied dual area MG system is shown in Figure 26. The FOTID controller has a sharp frequency reverberation up to 0.141 Hz and 0.123 Hz in areas a and b , respectively, at the wind integration instant. The TI/FOTID controller presents a large peak frequency diffraction to 0.0826 Hz at area a and 0.0524 Hz at area b when there is an upsurge in active power from the wind farm due to its uncertainty velocity. The TD/FOTID gave satisfactory results compared with FOTID and TI/FOTID controllers. It can dampen the frequency perversion at 0.052 Hz at area a and 0.0198 Hz at area b . On the contrary, the proposed CC 1+TD/FOTIDF control technique manifested an outstanding performance against wind uncertainty. It can reduce the deviation in system frequency to 0.004 Hz and 0.001 Hz in both areas. This is because the CC 1+TD/FOTIDF does not have a phase lag in responding to different generation and load disturbances compared to other single-loop controllers. Furthermore, the proposed cascaded controllers proved their superiority to the fast charge and discharge from the EVs in both areas. Figure 27 shows that the control signal from the proposed technique accomplished reducing the power from the thermal and hydraulic powers with a quick discharge from the EV system, especially at instants of increasing/decreasing the PV power and integration of the wind farm to the dual area MG system comparing with other conventional and fractional controllers.



(a)



(b)



(c)

Figure 23. Performance results at Scenario 4. (a) Δf_a (P.U.); (b) Δf_b (P.U.); (c) ΔP_{tie} (P.U.).

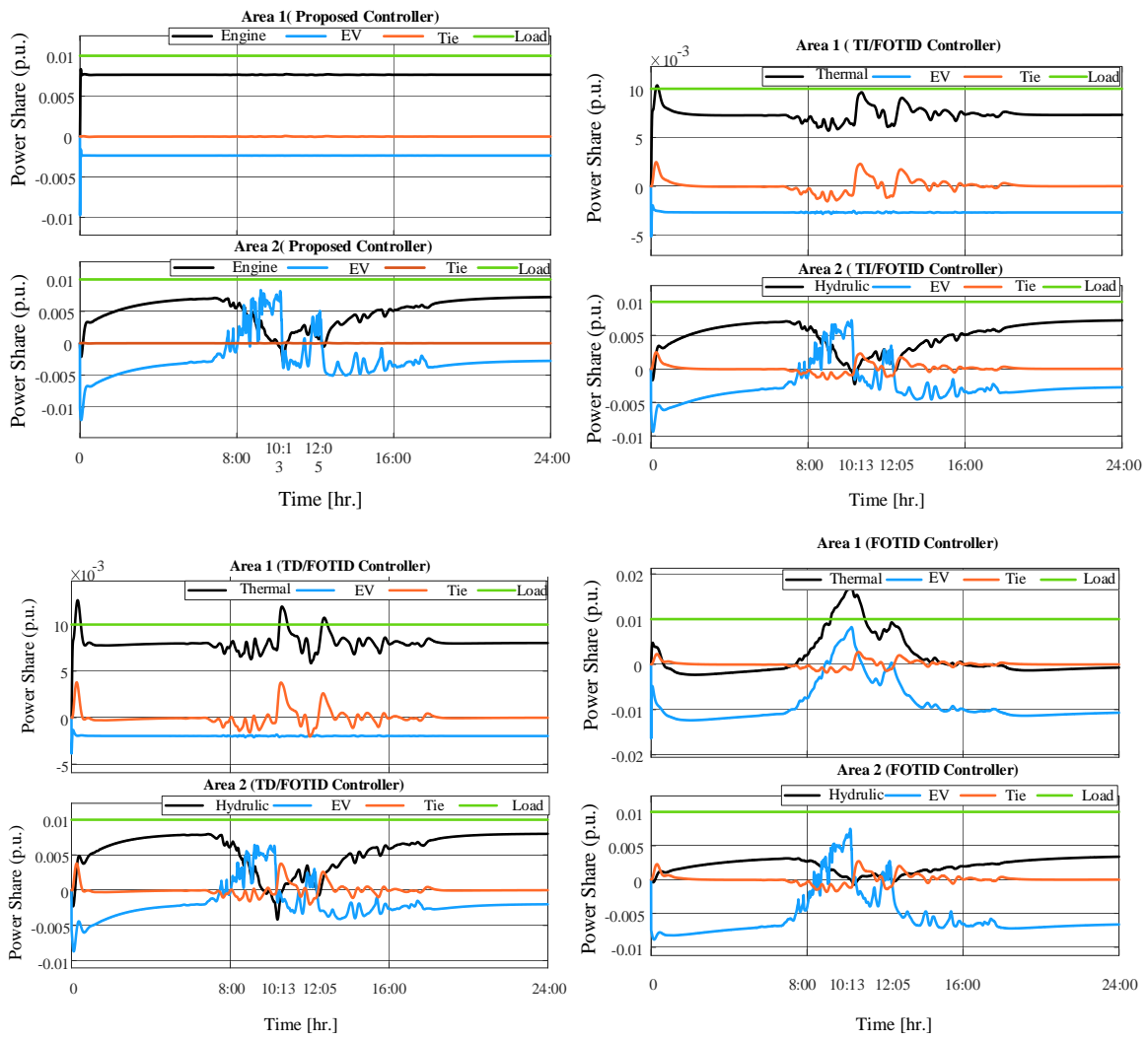


Figure 24. Performance of generators and EVs at Scenario 4.

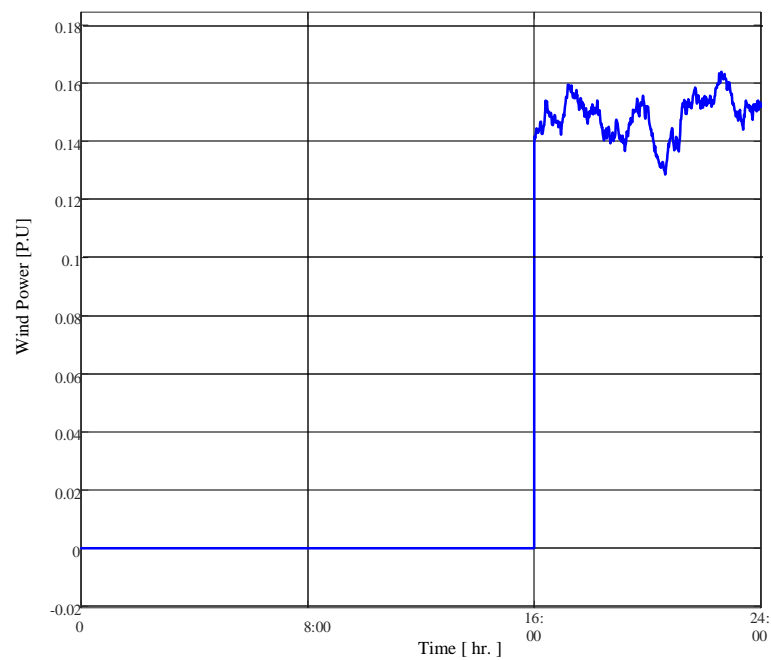
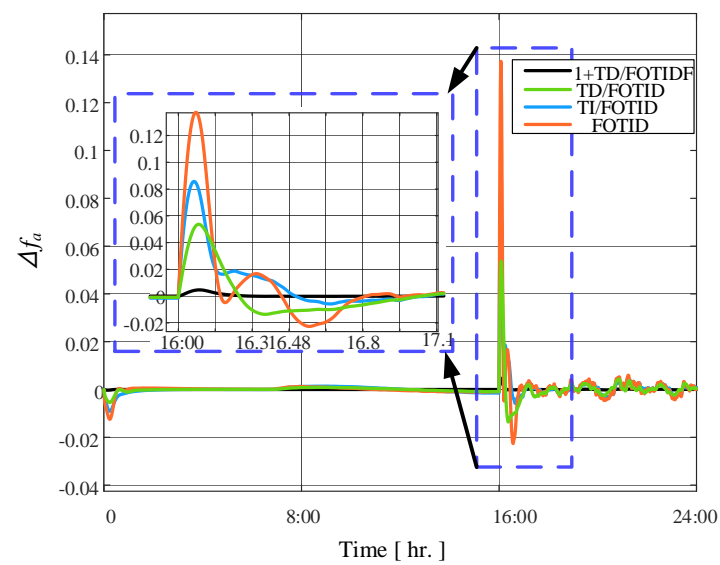
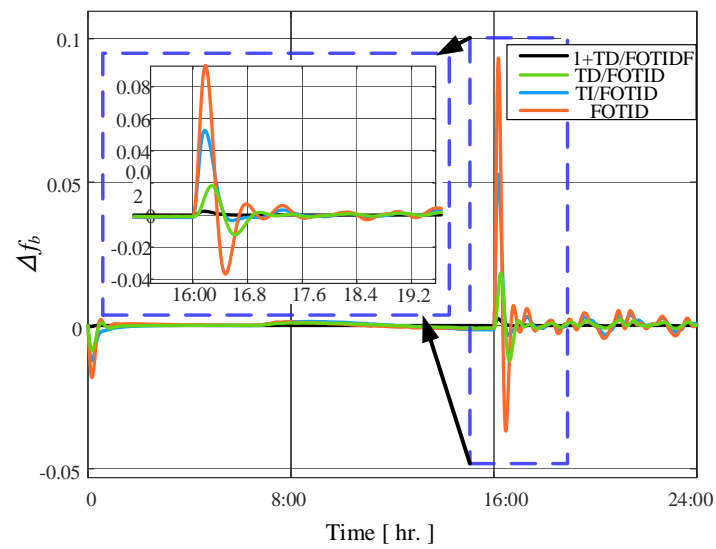


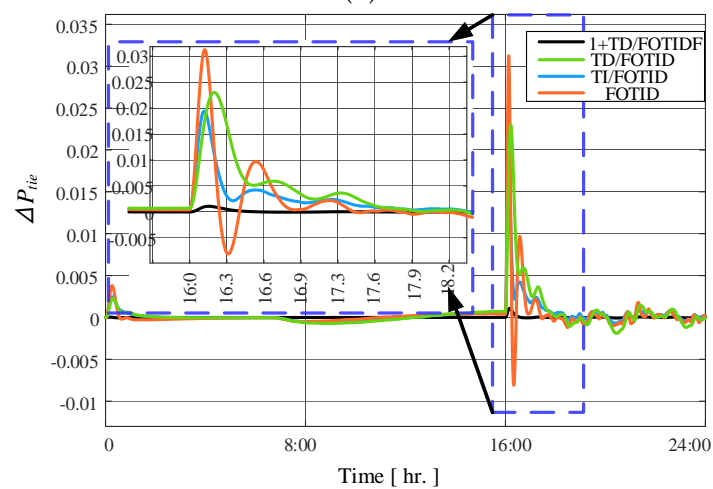
Figure 25. Wind generation characteristics of scenario 5.



(a)



(b)



(c)

Figure 26. Performance results at Scenario 5. (a) Δf_a (P.U.); (b) Δf_b (P.U.); (c) ΔP_{tie} (P.U.).

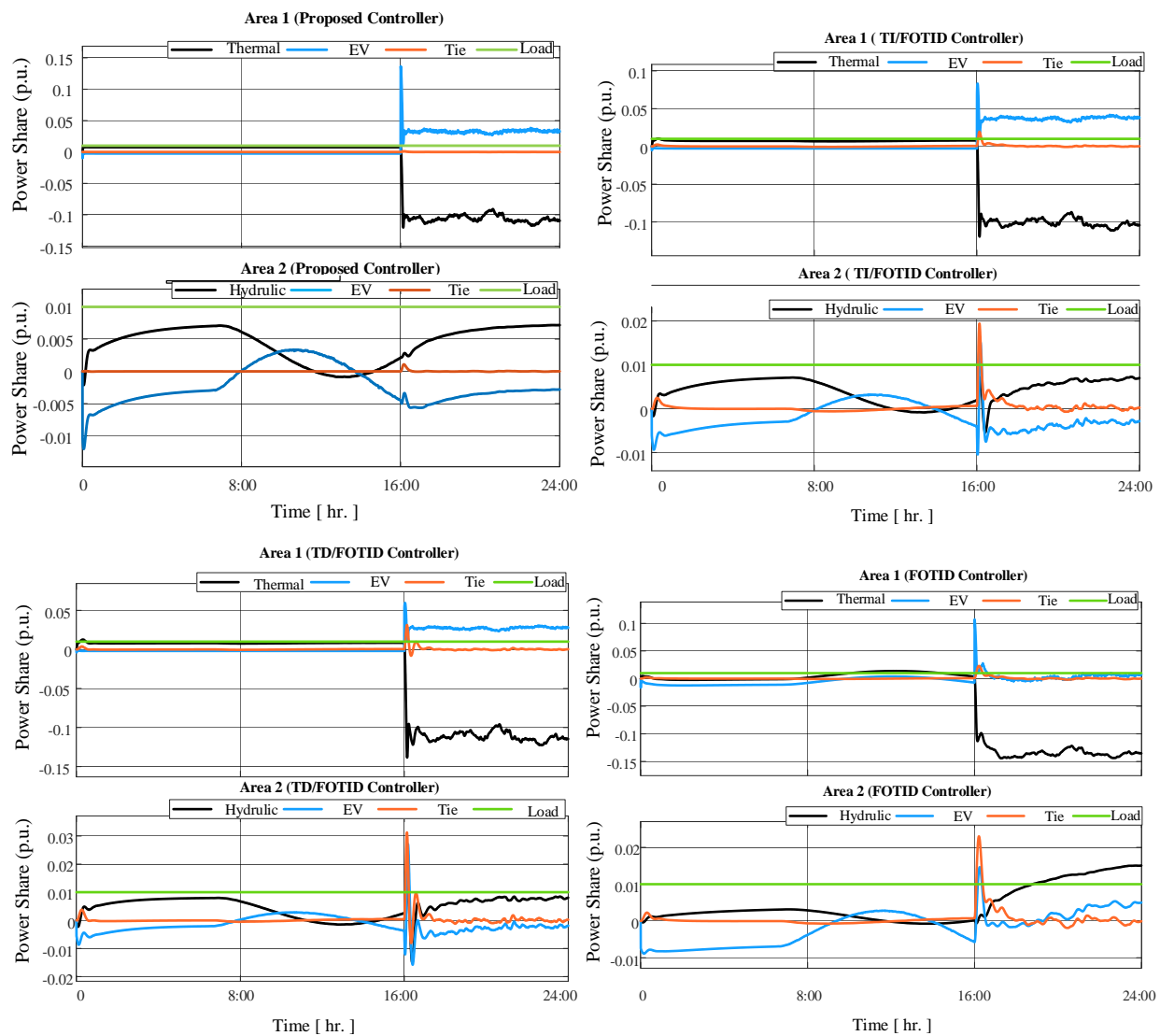


Figure 27. Performance of generators and EVs at Scenario 5.

6. Conclusions

The integration of improperly controlled renewable energy resources and electric vehicles into the power system might result in frequency fluctuations, leading to desynchronization and ultimately compromising the stability of the power system. Numerous LFC techniques have been proposed in the literature to regulate the system frequency at a stable level. The paper introduces an improved version of a PID controller with fractional order. The proposed controller is a cascaded controller comprising a 1+TD inner controller and an outer controller with a FOTIDF controller, resulting in a 1+TD/FOTIDF controller. The proposed controller exhibits an effective capacity to reject both existing generations and load disturbances, hence enhancing the stability of the multi-microgrids under imbalanced power conditions. Moreover, the proposed 1+TD/FOTIDF controller effectively manages the involvement of the electric vehicle's batteries and helps mitigate disruptions in the power system frequency. Furthermore, a new MLC optimization approach is introduced to enhance the parameters of the 1+TD/FOTIDF controller in the presented areas. The proposed MLCA algorithm accurately selected the best parameters of the 1+TD/FOTIDF controller. Different generation scenarios of the PV plant based on real solar radiation data have been applied to test the proposed controller together with the proposed MLC optimization technique. Moreover, different WT generation and loading scenarios have been used to examine the proposed techniques. The simulation results under all scenarios

prove the accuracy and the high functionality of the proposed 1+TD/FOTIDF controller to mitigate the frequency disturbances and keep the power system stable even under sudden changes in the PV and WT generations and loads. Future work includes the application of the proposed controller and modified optimization algorithm on other power system case studies with different generation unit types, different energy storage devices, and/or loading profiles.

Author Contributions: Methodology, A.M.N.; Software, S.Z.A., A.S.A. and M.E.; Validation, M.E.; Formal analysis, A.M.N. and M.A.; Investigation, M.H.A. and S.Z.A.; Data curation, A.M.N. and S.Z.A.; Writing—original draft, M.A.; Writing—review & editing, E.A.M.; Visualization, A.S.A.; Supervision, M.H.A.; Project administration, M.H.A.; Funding acquisition, M.H.A. All authors have read and agreed to the published version of the manuscript.

Funding: The authors extend their appreciation to Prince Sattam bin Abdulaziz University for funding this research work through the project number (PSAU/2023/01/9076).

Data Availability Statement: No new data were created or analyzed in this study. Data sharing is not applicable to this article.

Conflicts of Interest: The authors declare no conflicts of interest.

References

- Ozkop, E.; Altas, I.H.; Sharaf, A.M. Load Frequency Control in Four Area Power Systems Using Fuzzy Logic PI Controller. In Proceedings of the 16th National Power Systems Conference, Hyderabad, India, 15–17 December 2010.
- Khodabakhshian, A.; Hooshmand, R. A new PID controller design for automatic generation control of hydro power systems. *Int. J. Electr. Power Energy Syst.* **2010**, *32*, 375–382. [[CrossRef](#)]
- Ibraheem.; Kumar, P.; Kothari, D. Recent Philosophies of Automatic Generation Control Strategies in Power Systems. *IEEE Trans. Power Syst.* **2005**, *20*, 346–357. [[CrossRef](#)]
- Morsali, J.; Zare, K.; Tarafdar Hagh, M. MGSO optimised TID-based GCSC damping controller in coordination with AGC for diverse-GENCOs multi-DISCOs power system with considering GDB and GRC non-linearity effects. *IET Gener. Transm. Distrib.* **2017**, *11*, 193–208. [[CrossRef](#)]
- Khooban, M.H.; Niknam, T. A new intelligent online fuzzy tuning approach for multi-area load frequency control: Self Adaptive Modified Bat Algorithm. *Int. J. Electr. Power Energy Syst.* **2015**, *71*, 254–261. [[CrossRef](#)]
- Lal, D.K.; Barisal, A. Comparative performances evaluation of FACTS devices on AGC with diverse sources of energy generation and SMES. *Cogent Eng.* **2017**, *4*, 1318466. [[CrossRef](#)]
- Tasnin, W.; Saikia, L.C. Performance comparison of several energy storage devices in deregulated AGC of a multi-area system incorporating geothermal power plant. *IET Renew. Power Gener.* **2018**, *12*, 761–772. [[CrossRef](#)]
- Rajbongshi, R.; Saikia, L.C. Combined control of voltage and frequency of multi-area multisource system incorporating solar thermal power plant using LSA optimised classical controllers. *IET Gener. Transm. Distrib.* **2017**, *11*, 2489–2498. [[CrossRef](#)]
- Tasnin, W.; Saikia, L.C. Maiden application of an sine–cosine algorithm optimised FO cascade controller in automatic generation control of multi-area thermal system incorporating dish–Stirling solar and geothermal power plants. *IET Renew. Power Gener.* **2018**, *12*, 585–597. [[CrossRef](#)]
- Ghasemi-Marzbali, A. Multi-area multi-source automatic generation control in deregulated power system. *Energy* **2020**, *201*, 117667. [[CrossRef](#)]
- Nosratabadi, S.M.; Bornapour, M.; Gharaei, M.A. Grasshopper optimization algorithm for optimal load frequency control considering Predictive Functional Modified PID controller in restructured multi-resource multi-area power system with Redox Flow Battery units. *Control Eng. Pract.* **2019**, *89*, 204–227. [[CrossRef](#)]
- Zhu, Q.; Jiang, L.; Yao, W.; Zhang, C.K.; Luo, C. Robust Load Frequency Control with Dynamic Demand Response for Deregulated Power Systems Considering Communication Delays. *Electr. Power Compon. Syst.* **2016**, *45*, 75–87. [[CrossRef](#)]
- Naveed, A.; Sonmez, S.; Ayasun, S. Stability Regions in the Parameter Space of PI Controller for LFC System with EVs Aggregator and Incommensurate Time Delays. In Proceedings of the 2019 1st Global Power, Energy and Communication Conference (GPECOM), Nevsehir, Turkey, 12–15 June 2019; IEEE: Piscataway, NJ, USA, 2019. [[CrossRef](#)]
- Elgerd, O.; Fosha, C. Optimum Megawatt-Frequency Control of Multiarea Electric Energy Systems. *IEEE Trans. Power Appar. Syst.* **1970**, *PAS-89*, 556–563. [[CrossRef](#)]
- Linton, T. Automatic Generation Control of Electric Energy Systems—A Simulation Study. *IEEE Trans. Syst. Man Cybern.* **1973**, *SMC-3*, 403–405. [[CrossRef](#)]
- Elgerd, O.I. *Electric Energy Systems Theory*, 2nd ed.; McGraw Hill Higher Education: Maidenhead, UK, 1983.
- Saha, D.; Saikia, L.C. Performance of FACTS and energy storage devices in a multi area wind-hydro-thermal system employed with SFS optimized I-PDF controller. *J. Renew. Sustain. Energy* **2017**, *9*, 024103. [[CrossRef](#)]

18. Raju, M.; Saikia, L.C.; Sinha, N. Load frequency control of a multi-area system incorporating distributed generation resources, gate controlled series capacitor along with high-voltage direct current link using hybrid ALO-pattern search optimised fractional order controller. *IET Renew. Power Gener.* **2018**, *13*, 330–341. [[CrossRef](#)]
19. Mohanty, B.; Panda, S.; Hota, P. Controller parameters tuning of differential evolution algorithm and its application to load frequency control of multi-source power system. *Int. J. Electr. Power Energy Syst.* **2014**, *54*, 77–85. [[CrossRef](#)]
20. Kumari, S.; Shankar, G. Maiden application of cascade tilt-integral-derivative controller in load frequency control of deregulated power system. *Int. Trans. Electr. Energy Syst.* **2019**, *30*, e12257. [[CrossRef](#)]
21. Dutta, A.; Debbarma, S. Frequency Regulation in Deregulated Market Using Vehicle-to-Grid Services in Residential Distribution Network. *IEEE Syst. J.* **2018**, *12*, 2812–2820. [[CrossRef](#)]
22. Prasad, S.; Purwar, S.; Kishor, N. Load frequency regulation using observer based non-linear sliding mode control. *Int. J. Electr. Power Energy Syst.* **2019**, *104*, 178–193. [[CrossRef](#)]
23. Saha, A.; Saikia, L.C. Utilisation of ultra-capacitor in load frequency control under restructured STPP-thermal power systems using WOA optimised PIDN-FOPD controller. *IET Gener. Transm. Distrib.* **2017**, *11*, 3318–3331. [[CrossRef](#)]
24. Saha, A.; Saikia, L.C. Combined application of redox flow battery and DC link in restructured AGC system in the presence of WTS and DSTS in distributed generation unit. *IET Gener. Transm. Distrib.* **2018**, *12*, 2072–2085. [[CrossRef](#)]
25. Ram Babu, N.; Saikia, L.C. AGC of a multiarea system incorporating accurate HVDC and precise wind turbine systems. *Int. Trans. Electr. Energy Syst.* **2019**, *30*, e12277. [[CrossRef](#)]
26. Zare, K.; Hagh, M.T.; Morsali, J. Effective oscillation damping of an interconnected multi-source power system with automatic generation control and TCSC. *Int. J. Electr. Power Energy Syst.* **2015**, *65*, 220–230. [[CrossRef](#)]
27. Tasnin, W.; Saikia, L.C.; Raju, M. Deregulated AGC of multi-area system incorporating dish-Stirling solar thermal and geothermal power plants using fractional order cascade controller. *Int. J. Electr. Power Energy Syst.* **2018**, *101*, 60–74. [[CrossRef](#)]
28. Verma, Y.P.; Kumar, A. Load frequency control in deregulated power system with wind integrated system using fuzzy controller. *Front. Energy* **2012**, *7*, 245–254. [[CrossRef](#)]
29. Shiva, C.K.; Mukherjee, V. A novel quasi-oppositional harmony search algorithm for AGC optimization of three-area multi-unit power system after deregulation. *Eng. Sci. Technol. Int. J.* **2016**, *19*, 395–420. [[CrossRef](#)]
30. Gondaliya, S.; Arora, M.K. Automatic Generation Control of Multi Area Power Plants with the Help of Advanced Controller. *Int. J. Eng. Res. Technol.* **2015**, *V4*, 470–474. [[CrossRef](#)]
31. Haes Alhelou, H.; Hamedani Golshan, M.E.; Hajiakbari Fini, M. Wind Driven Optimization Algorithm Application to Load Frequency Control in Interconnected Power Systems Considering GRC and GDB Nonlinearities. *Electr. Power Compon. Syst.* **2018**, *46*, 1223–1238. [[CrossRef](#)]
32. Gulzar, M.M.; Iqbal, M.; Shahzad, S.; Muqet, H.A.; Shahzad, M.; Hussain, M.M. Load Frequency Control (LFC) Strategies in Renewable Energy-Based Hybrid Power Systems: A Review. *Energies* **2022**, *15*, 3488. [[CrossRef](#)]
33. Guha, D.; Roy, P.K.; Banerjee, S. Symbiotic organism search algorithm applied to load frequency control of multi-area power system. *Energy Syst.* **2017**, *9*, 439–468. [[CrossRef](#)]
34. Guha, D.; Roy, P.K.; Banerjee, S. Application of backtracking search algorithm in load frequency control of multi-area interconnected power system. *Ain Shams Eng. J.* **2018**, *9*, 257–276. [[CrossRef](#)]
35. Safi, S.J.; Tezcan, S.S.; Eke, I.; Farhad, Z. Gravitational Search Algorithm (GSA) based PID Controller Design for Two Area Multi-Source Power System Load Frequency Control (LFC). *Gazi Univ. J. Sci.* **2018**, *31*, 139–153.
36. Arora, K.; Kumar, A.; Kamboj, V.K.; Prashar, D.; Shrestha, B.; Joshi, G.P. Impact of Renewable Energy Sources into Multi Area Multi-Source Load Frequency Control of Interrelated Power System. *Mathematics* **2021**, *9*, 186. [[CrossRef](#)]
37. Saxena, A.; Shankar, R. Improved load frequency control considering dynamic demand regulated power system integrating renewable sources and hybrid energy storage system. *Sustain. Energy Technol. Assess.* **2022**, *52*, 102245. [[CrossRef](#)]
38. Xu, C.; Ou, W.; Pang, Y.; Cui, Q.; Rahman, M.u.; Farman, M.; Ahmad, S.; Zeb, A. Hopf Bifurcation Control of a Fractional-Order Delayed Turbidostat Model via a Novel Extended Hybrid Controller. *Match Commun. Math. Comput. Chem.* **2023**, *91*, 367–413. [[CrossRef](#)]
39. Eshaghi, S.; Khoshsiar Ghaziani, R.; Ansari, A. Hopf bifurcation, chaos control and synchronization of a chaotic fractional-order system with chaos entanglement function. *Math. Comput. Simul.* **2020**, *172*, 321–340. [[CrossRef](#)]
40. Kaslik, E.; Rădulescu, I.R. Stability and bifurcations in fractional-order gene regulatory networks. *Appl. Math. Comput.* **2022**, *421*, 126916. [[CrossRef](#)]
41. Irudayaraj, A.X.R.; Wahab, N.I.A.; Premkumar, M.; Radzi, M.A.M.; Sulaiman, N.B.; Veerasamy, V.; Farade, R.A.; Islam, M.Z. Renewable sources-based automatic load frequency control of interconnected systems using chaotic atom search optimization. *Appl. Soft Comput.* **2022**, *119*, 108574. [[CrossRef](#)]
42. Kong, F.; Li, J.; Yang, D. Multi-Area Load Frequency Control of Hydro-Thermal-Wind Power Based on Improved Grey Wolf Optimization Algorithm. *Elektron. Elektrotehnika* **2020**, *26*, 32–39. [[CrossRef](#)]
43. Khadanga, R.K.; Kumar, A.; Panda, S. A modified Grey Wolf Optimization with Cuckoo Search Algorithm for load frequency controller design of hybrid power system. *Appl. Soft Comput.* **2022**, *124*, 109011. [[CrossRef](#)]
44. Soliman, A.M.A.; Bahaa, M.; Mehanna, M.A. PSO tuned interval type-2 fuzzy logic for load frequency control of two-area multi-source interconnected power system. *Sci. Rep.* **2023**, *13*, 8724. [[CrossRef](#)]

45. Kumar, R.; Sikander, A. A novel load frequency control of multi area non-reheated thermal power plant using fuzzy PID cascade controller. *Sādhanā* **2023**, *48*, 25. [[CrossRef](#)]
46. Yousef, M.Y.; Mosa, M.A.; Ali, A.; Ghany, A.; Ghany, M. Load frequency control for power system considering parameters variation using parallel distributed compensator based on Takagi-Sugino fuzzy. *Electr. Power Syst. Res.* **2023**, *220*, 109352. [[CrossRef](#)]
47. Saikia, N.; Das, N.K. Load Frequency Control of a Two Area Multi-source Power System with Electric Vehicle. *J. Control. Autom. Electr. Syst.* **2022**, *34*, 394–406. [[CrossRef](#)]
48. El-Sehiemy, R.; Shaheen, A.; Ginidi, A.; Al-Gahtani, S.F. Proportional-Integral-Derivative Controller Based-Artificial Rabbits Algorithm for Load Frequency Control in Multi-Area Power Systems. *Fractal Fract.* **2023**, *7*, 97. [[CrossRef](#)]
49. Kumari, N.; Gill, A.; Singh, M. Two-Area Power System Load Frequency Regulation Using ANFIS and Genetic Algorithm. In Proceedings of the 2023 4th International Conference for Emerging Technology (INCET), Belgaum, India, 26–28 May 2023; IEEE: Piscataway, NJ, USA, 2023. [[CrossRef](#)]
50. Halmous, A.; Oubbati, Y.; Lahdeb, M.; Arif, S. Design a new cascade controller PD-P-PID optimized by marine predators algorithm for load frequency control. *Soft Comput.* **2023**, *27*, 9551–9564. [[CrossRef](#)]
51. Alhejji, A.; Ahmed, N.; Ebeed, M.; Sayed, K.; Refai, A. A Robust Cascaded Controller for Load Frequency Control in Renewable Energy Integrated Microgrid Containing PEV. *Int. J. Renew. Energy Res.* **2023**, *13*, 423–433. [[CrossRef](#)]
52. Gulzar, M.M.; Sibtain, D.; Khalid, M. Cascaded Fractional Model Predictive Controller for Load Frequency Control in Multiarea Hybrid Renewable Energy System with Uncertainties. *Int. J. Energy Res.* **2023**, *2023*, 5999997. [[CrossRef](#)]
53. Duman, S.; Balci, Y. Improvement of Load Frequency Control for Two-Area Modern Power Systems Involving Renewable Energy Sources Using a Novel Cascade Controller. 2023. Available online: <https://www.researchsquare.com/article/rs-3215487/v1> (accessed on 15 January 2024).
54. El-Sousy, F.F.M.; Aly, M.; Alqahtani, M.H.; Aljumah, A.S.; Almutairi, S.Z.; Mohamed, E.A. New Cascaded 1+PII2D/FOPID Load Frequency Controller for Modern Power Grids including Superconducting Magnetic Energy Storage and Renewable Energy. *Fractal Fract.* **2023**, *7*, 672. [[CrossRef](#)]
55. Ahmed, E.M.; Mohamed, E.A.; Selim, A.; Aly, M.; Alsadi, A.; Alhosaini, W.; Alnuman, H.; Ramadan, H.A. Improving load frequency control performance in interconnected power systems with a new optimal high degree of freedom cascaded FOTPID-TIDF controller. *Ain Shams Eng. J.* **2023**, *14*, 102207. [[CrossRef](#)]
56. Hassan, A.; Aly, M.M.; Alharbi, M.A.; Selim, A.; Alamri, B.; Aly, M.; Elmelegi, A.; Khamies, M.; Mohamed, E.A. Optimized Multiloop Fractional-Order Controller for Regulating Frequency in Diverse-Sourced Vehicle-to-Grid Power Systems. *Fractal Fract.* **2023**, *7*, 864. [[CrossRef](#)]
57. Elkasem, A.H.; Khamies, M.; Hassan, M.H.; Nasrat, L.; Kamel, S. Utilizing controlled plug-in electric vehicles to improve hybrid power grid frequency regulation considering high renewable energy penetration. *Int. J. Electr. Power Energy Syst.* **2023**, *152*, 109251. [[CrossRef](#)]
58. Villalva, M.G.; Gazoli, J.R.; Filho, E.R. Modeling and circuit-based simulation of photovoltaic arrays. In Proceedings of the 2009 Brazilian Power Electronics Conference, Bonito-Mato Grosso do Sul, Brazil, 27 September–1 October 2009; IEEE: Piscataway, NJ, USA, 2009. [[CrossRef](#)]
59. Walker, G.R. Evaluating MPPT Converter Topologies Using a Matlab PV Model. *J. Electr. Electron. Eng. Aust.* **2001**, *21*, 49–55.
60. Arya, Y. Impact of ultra-capacitor on automatic generation control of electric energy systems using an optimal FFOID controller. *Int. J. Energy Res.* **2019**, *43*, 8765–8778. [[CrossRef](#)]
61. Micev, M.; Čalasan, M.; Oliva, D. Fractional Order PID Controller Design for an AVR System Using Chaotic Yellow Saddle Goatfish Algorithm. *Mathematics* **2020**, *8*, 1182. [[CrossRef](#)]
62. Dulf, E.H. Simplified Fractional Order Controller Design Algorithm. *Mathematics* **2019**, *7*, 1166. [[CrossRef](#)]
63. Motorga, R.; Mureşan, V.; Ungureşan, M.L.; Abrudean, M.; Vălean, H.; Clitan, I. Artificial Intelligence in Fractional-Order Systems Approximation with High Performances: Application in Modelling of an Isotopic Separation Process. *Mathematics* **2022**, *10*, 1459. [[CrossRef](#)]
64. Benbouhenni, H.; Zellouma, D.; Bizon, N.; Colak, I. A new PI(1 +PI) controller to mitigate power ripples of a variable-speed dual-rotor wind power system using direct power control. *Energy Rep.* **2023**, *10*, 3580–3598. [[CrossRef](#)]
65. Choudhary, R.; Rai, J.; Arya, Y. FOPTID+1 controller with capacitive energy storage for AGC performance enrichment of multi-source electric power systems. *Electr. Power Syst. Res.* **2023**, *221*, 109450. [[CrossRef](#)]
66. Houssein, E.H.; Oliva, D.; Samee, N.A.; Mahmoud, N.F.; Emam, M.M. Liver Cancer Algorithm: A novel bio-inspired optimizer. *Comput. Biol. Med.* **2023**, *165*, 107389. [[CrossRef](#)]
67. Kahraman, H.T.; Aras, S.; Gedikli, E. Fitness-distance balance (FDB): A new selection method for meta-heuristic search algorithms. *Knowl.-Based Syst.* **2020**, *190*, 105169. [[CrossRef](#)]
68. Hachemi, A.T.; Sadaoui, F.; Arif, S.; Saim, A.; Ebeed, M.; Kamel, S.; Jurado, F.; Mohamed, E.A. Modified reptile search algorithm for optimal integration of renewable energy sources in distribution networks. *Energy Sci. Eng.* **2023**, *11*, 4635–4665. [[CrossRef](#)]
69. Adhikari, A.; Jurado, F.; Naetiladdanon, S.; Sangswang, A.; Kamel, S.; Ebeed, M. Stochastic optimal power flow analysis of power system with renewable energy sources using Adaptive Lightning Attachment Procedure Optimizer. *Int. J. Electr. Power Energy Syst.* **2023**, *153*, 109314. [[CrossRef](#)]

70. Ebeed, M.; Mostafa, A.; Aly, M.M.; Jurado, F.; Kamel, S. Stochastic optimal power flow analysis of power systems with wind/PV/TCSC using a developed Runge Kutta optimizer. *Int. J. Electr. Power Energy Syst.* **2023**, *152*, 109250. [[CrossRef](#)]
71. Guvenc, U.; Duman, S.; Kahraman, H.T.; Aras, S.; Katu, M. Fitness–Distance Balance based adaptive guided differential evolution algorithm for security-constrained optimal power flow problem incorporating renewable energy sources. *Appl. Soft Comput.* **2021**, *108*, 107421. [[CrossRef](#)]
72. Sharifi, M.R.; Akbarifard, S.; Qaderi, K.; Madadi, M.R. Developing MSA Algorithm by New Fitness–Distance–Balance Selection Method to Optimize Cascade Hydropower Reservoirs Operation. *Water Resour. Manag.* **2021**, *35*, 385–406. [[CrossRef](#)]
73. Xia, J.; Zhang, H.; Li, R.; Wang, Z.; Cai, Z.; Gu, Z.; Chen, H.; Pan, Z. Adaptive Barebones Salp Swarm Algorithm with Quasi-oppositional Learning for Medical Diagnosis Systems: A Comprehensive Analysis. *J. Bionic Eng.* **2022**, *19*, 240–256. [[CrossRef](#)]
74. Chaudhuri, A.; Sahu, T.P. Multi-objective feature selection based on quasi-oppositional based Jaya algorithm for microarray data. *Knowl.-Based Syst.* **2022**, *236*, 107804. [[CrossRef](#)]
75. Gharehchopogh, F.S.; Nadimi-Shahraki, M.H.; Barshandeh, S.; Abdollahzadeh, B.; Zamani, H. CQFFA: A Chaotic Quasi-oppositional Farmland Fertility Algorithm for Solving Engineering Optimization Problems. *J. Bionic Eng.* **2022**, *20*, 158–183. [[CrossRef](#)]
76. Kandan, M.; Krishnamurthy, A.; Selvi, S.A.M.; Sikkandar, M.Y.; Aboamer, M.A.; Tamilvizhi, T. Quasi oppositional Aquila optimizer-based task scheduling approach in an IoT enabled cloud environment. *J. Supercomput.* **2022**, *78*, 10176–10190. [[CrossRef](#)]
77. Latchoumi, T.P.; Parthiban, L. Quasi Oppositional Dragonfly Algorithm for Load Balancing in Cloud Computing Environment. *Wirel. Pers. Commun.* **2021**, *122*, 2639–2656. [[CrossRef](#)]
78. Guha, D.; Roy, P.K.; Banerjee, S. Quasi-oppositional JAYA optimized 2-degree-of-freedom PID controller for load-frequency control of interconnected power systems. *Int. J. Model. Simul.* **2020**, *42*, 63–85. [[CrossRef](#)]
79. Marzouk, R.; Alzahrani, J.S.; Alrowais, F.; Al-Wesabi, F.N.; Hamza, M.A. Quasi-oppositional wild horse optimization based multi-agent path finding scheme for real time IoT systems. *Expert Syst.* **2022**, *39*, e13112. [[CrossRef](#)]
80. Rahnamayan, S.; Tizhoosh, H.R.; Salama, M.M. Opposition versus randomness in soft computing techniques. *Appl. Soft Comput.* **2008**, *8*, 906–918. [[CrossRef](#)]
81. Kapitaniak, T. Continuous control and synchronization in chaotic systems. *Chaos Solitons Fractals* **1995**, *6*, 237–244. [[CrossRef](#)]
82. Sayed, G.I.; Khoriba, G.; Haggag, M.H. A novel chaotic salp swarm algorithm for global optimization and feature selection. *Appl. Intell.* **2018**, *48*, 3462–3481. [[CrossRef](#)]
83. Abdel-Basset, M.; El-Shahat, D.; Jameel, M.; Abouhawwash, M. Exponential distribution optimizer (EDO): A novel math-inspired algorithm for global optimization and engineering problems. *Artif. Intell. Rev.* **2023**, *56*, 9329–9400. [[CrossRef](#)]
84. Trojovska, E.; Dehghani, M.; Trojovsky, P. Zebra Optimization Algorithm: A New Bio-Inspired Optimization Algorithm for Solving Optimization Algorithm. *IEEE Access* **2022**, *10*, 49445–49473. [[CrossRef](#)]
85. Seyyedabbasi, A.; Kiani, F. Sand Cat swarm optimization: A nature-inspired algorithm to solve global optimization problems. *Eng. Comput.* **2022**, *39*, 2627–2651. [[CrossRef](#)]
86. Eberhart, R.; Kennedy, J. A new optimizer using particle swarm theory. In Proceedings of the MHS'95. Proceedings of the Sixth International Symposium on Micro Machine and Human Science, Nagoya, Japan, 4–6 October 1995; MHS-95. IEEE: Piscataway, NJ, USA, 1995. [[CrossRef](#)]
87. Mirjalili, S. SCA: A Sine Cosine Algorithm for solving optimization problems. *Knowl.-Based Syst.* **2016**, *96*, 120–133. [[CrossRef](#)]
88. Derrac, J.; García, S.; Molina, D.; Herrera, F. A practical tutorial on the use of nonparametric statistical tests as a methodology for comparing evolutionary and swarm intelligence algorithms. *Swarm Evol. Comput.* **2011**, *1*, 3–18. [[CrossRef](#)]
89. Wood, J. CCTV Ergonomics: Case Studies and Practical Guidance. In *Meeting Diversity in Ergonomics*; Elsevier: Amsterdam, The Netherlands, 2007; pp. 271–287. [[CrossRef](#)]

Disclaimer/Publisher's Note: The statements, opinions and data contained in all publications are solely those of the individual author(s) and contributor(s) and not of MDPI and/or the editor(s). MDPI and/or the editor(s) disclaim responsibility for any injury to people or property resulting from any ideas, methods, instructions or products referred to in the content.